EUROPEAN ORGANIZATION FOR NUCLEAR RESEARCH

CERN-EP/89-53
12 April 1989

A DETAILED STUDY OF THE PERFORMANCE OF THE URANIUM-GAS SAMPLING CALORIMETER

L3 Collaboration,
CERN, Geneva, Switzerland

A. Arefiev[1)], T. Azemoon[2)], R. Bal[2)], S. Burov[1)], M. Capell[2)], H.S. Chen[3)],
M. Chen[4)], M. Chumakov[1)], Yu. Galaktionov[1)], S. Goldfarb[2)], Z.F. Gong[5)], A. Gordeev[1)],
Yu. Gorodkov[1)], L.W. Jones[2)], Yu. Kamyshkov[1)], A. Klimentov[1)], V. Koutsenko[1)], A. Kunin[1)],
P. Lecomte[6)], P. LeCoultre[6)], J. Lettry[6)], Z.R. Lin[6)], Y.S. Lu[3)], A. Malinin[1)],
G.B. Mills[2)], V. Morgunov[1)], V. Plyaskin[1)], V. Pojidaev[1)], B.P. Roe[2)], A. Rozhkov[1)],
A. Savin[1)], S. Shevchenko[1)], V. Shevchenko[1)], K. Shmakov[1)], V. Shoutko[1)], E. Shumilov[1)],
B. Spiess[6)], E. Tarkovsky[1)], V. Tchoudakov[1)], S.C.C. Ting[4)], K.L. Tung[3)],
J. Ulbricht[7)] and I. Vorobiev[1)]

ABSTRACT

Results of experimental studies of the performance of the uranium calorimeter with gas sampling detectors are presented. There is further evidence showing the importance of the contribution of the neutron component of a hadronic shower to the detected signal. The response and the resolution of the uranium calorimeter are measured in the momentum range 0.3–6.0 GeV/c for the different incident particles and different gases that are used in the detectors. For a calorimeter structure with double-gas-detector layers, the correlation between signals from two calorimeters formed by chambers filled with different gas mixtures is measured. The topics that are relevant to the performance of the L3 uranium-gas sampling calorimeter — such as its operation in the magnetic field, the energy dependence of muon response, the uranium noise, as well as the electronics optimization — are discussed.

(Submitted to Nuclear Instruments and Methods in Physics Research)

---

1) Institute for Theoretical and Experimental Physics, Moscow, USSR.
2) University of Michigan, Ann Arbor, Mich., USA.
3) Institute of High-Energy Physics, Academia Sinica, Beijing, People's Republic of China.
4) Massachusetts Institute of Technology, Cambridge, Mass., USA.
5) World Lab. (FBLJA) and University of Science and Technology of China, Hefei, People's Republic of China.
6) Eidgenossische Technische Hochschule, Zurich, Switzerland.
7) Paul Scherrer Institute, Würenlingen, Switzerland.

1. INTRODUCTION

The performances of the prototypes of a uranium sampling hadron calorimeter with gaseous detector readout have been extensively studied within the L3 Collaboration [1–5]. In our previous publication [5], we reported the results of ITEP Proton Synchrotron (PS) beam tests of a prototype with 4.5 mm uranium plates and wire proportional chambers made of brass tubes, 6×12 mm^2 inner dimensions, filled with various gas mixtures.

In this paper we present the results of further studies on the same topic. Section 2 briefly describes the structure of the calorimeter, the experimental set-up, the data analysis and event selection procedures, as well as the accuracy of our measurements. In Section 3 we present the results of the performance of the calorimeter at different beam momenta in the range 0.3–6.0 GeV/c, for different incident particles, different gases, and various absorber structures.

The importance of the low-energy neutron component of the hadronic shower in a uranium–gas sampling calorimeter was discussed in ref. [5]. We have performed more detailed studies of the neutron component, and the results are presented in subsection 3.1. The performance of the calorimeter at low incident energies is discussed in subsection 3.2, and the energy resolution and relevant analysis procedures are presented in subsection 3.3. Some measurements were made with a double-chamber structure (i.e. two chambers were placed behind a single absorber) to study the correlation between chambers filled with different gas mixtures and the suppression of neutron 'spikes'. This is discussed in subsection 3.3.3.

Section 4 is devoted to some specific studies that are relevant to the performance of the L3 hadron calorimeter: the performance of the calorimeter in a magnetic field, simulating L3 conditions (4.1); the calorimeter response to muons (4.2); the uranium-noise contribution and optimization of the electronics (4.3).

2. THE CALORIMETER

2.1 Experimental set-up

The beam and experimental set-up, the construction and operation of the chambers, the 'slow' and 'fast' readout electronics, the calibration procedures and pion–electron–muon separation, have already been discussed in ref. [5]. Here we briefly describe the apparatus. The beam layout used is shown in fig. 1. The calorimeter had a modular structure. One module consisted of a uranium absorber plate, 4.5 mm thick, followed by a chamber with or without shielding. The module had a constant thickness (if not otherwise specified) independent of its internal structure. The shielding consisted of either 1 mm Cu or 2 mm Plexiglas plates on each side of the chamber. The total thickness of the calorimeter was approximately 4 absorption lengths. The calorimeter (absorber and chambers) had a 50×50 cm^2 transverse dimension.

Table 1 summarizes the different structures, gas mixtures, and other relevant parameters of the set-up used in the present study. With the 'fast' electronics readout, all 40 wires of each plane were combined in a single analog readout channel, whereas with the 'slow' electronics, every chamber plane had eight analog readout channels, each containing a group of five adjacent wires grouped together.

A number of hardware improvements were made to the set-up described in ref. [5]. These were as follows.

i) A second Cherenkov counter, filled with CO_2 gas, was installed in the beam for better electron–pion separation. Thus the contamination of pions in the electron trigger was below 1% in the whole momentum range.

ii) Using time-of-flight (TOF) measurements with a r.m.s. resolution of 0.7 ns over the 10 m distance between the two beam telescope counters C1 and C3, the separation of pions, protons, and deuterons below 3 GeV/c became possible. The TOF spectrum for a 2.08 GeV/c positive beam is shown in fig. 2.

iii) The momentum range was extended to 0.3–6.0 GeV/c. The linearity of the beam momentum with magnet settings was cross-checked with a Cherenkov lead-glass counter for the electrons in the whole momentum range. The absolute beam-momentum calibration was performed by TOF measurements at 1 GeV/c and, independently, by comparing the measured and the calculated ranges of the low-energy muons. The accuracy of the absolute beam-momentum calibration was about 1%.

iv) A trigger processor was used to allow for the simultaneous data-taking of the different incident particles and the calibration data in a desired proportion. Thus the effect of electronic drift and long-term instabilities was considerably reduced.

v) Occasionally, the amplification factors of readout channels were monitored with the random 'uranium-noise trigger' described in detail in ref. [6]. The accuracy of the method was 2–4%. Uniformity of amplification over the whole calorimeter was about 10% (r.m.s.), which has to be attributed mainly to differences in gas amplifications of the proportional tubes and, to a lesser extent, to the non-uniformity of the gain of the electronics. We did not introduce averaged intercalibration corrections for individual channels since, in every readout cell, several wires with different gas amplification were grouped together, and because such corrections did not improve the overall calorimeter resolution.

The chambers were operated in a proportional mode with several gas mixtures (table 1). The 'slow' and 'fast' electronics readout systems were both adjusted to match a gas gain of about 10^4. The typical values for the high voltage were 2800 V for iC_4H_{10} (isobutane), 2700 V for Ar (10%) + CO_2 (90%), and 1720 V for Ar (80%) + CO_2 (20%). By varying the high voltage within ±100 V around the working point, we checked that the ratios of responses of pions to electrons, and of electrons to muons, were constant at fixed beam energy. At the working high voltage, the mean value of the minimum-ionizing-particle signal per chamber was typically: 9 ADC channels for the fast electronics and all gas mixtures used; 25 ADC channels for the slow electronics and the Ar + CO_2 mixtures; 18 ADC channels for the slow electronics and isobutane. The ADC range was 10 bits for the fast electronics and 12 bits for the slow.

2.2 Data analysis

The pedestal data were collected simultaneously with the calorimeter response measurements. The pedestal values were measured during the beam spill with the chamber high voltage on, and were defined as the mean values of the corresponding distributions for individual or summed-up electronics channels without any cuts. A pedestal distribution had a tail, which was due to the U noise and the beam pile-up. The U-noise rate was approximately 30 counts per square centimetre and second, and the typical beam intensities were kept at around 10^4 per one-second spill. No coherent noise, other than beam pile-up, was observed. The cross-talk was checked to be below 1% for the fast electronics, and was not detectable for the slow electronics.

The calorimeter response was measured in units of 'mip'. This unit was defined as the mean value of a Gaussian fit to the total response for the 2 GeV/c muons divided by the number of chambers in the calorimeter.

The electrons were selected by two Cherenkov counters. The muons of momenta above 2 GeV/c were selected at the trigger level, since they traversed an additional iron absorber of two interaction lengths. For pion–proton–deuteron separation below 3 GeV/c, TOF information was used. The most difficult problem at low energies ($E_{kin} < 1$ GeV) was the separation of pions from muons that were also stopped in the calorimeter. Fine longitudinal and lateral segmentation of the calorimeter enabled us to use the detailed information on the shower development to overcome this difficulty. A comparison of the signals in each calorimeter plane with the reference spectrum obtained from the measurements with 2 GeV/c muons made it possible to calculate the value of a likelihood function. Applying an appropriate cut on this value and using the information about event topology, we obtained a good separation of low-energy pions from muons.

The electron response was defined as the sum of the amplitudes of the first 20 calorimeter planes, corresponding to more than 27 radiation lengths, whereas the muon, pion, proton, and deuteron responses were defined as the sum of the amplitudes of the whole calorimeter without any restriction or amplitude cut. Since the total electron response distributions were symmetric at all energies and for all gases, we used a Gaussian fit to these distributions to obtain the mean response and the value of the distribution width. For other particles, the response was calculated as the formal mean value of the corresponding distribution.

The ratio of the hadron to electron responses, as well as that of the muon to electron responses, was calculated at the same kinetic energy, i.e. the response of electrons with a given momentum was scaled down to the kinetic energy of hadrons with the same momentum. Note that in ref. [5] the pion-to-electron ratios were defined at the same momentum.

We used two definitions for the energy resolution: i) the r.m.s. of a distribution, and ii) the standard deviation (st. dev.) of a Gaussian fit to the distribution. The former is a correct statistical estimate, but experimentally it can be affected by beam pile-up effects and U noise. The latter is good only for symmetric distributions and is insensitive to the beam pile-up effects.

The ranges for stopping particles (muons, protons, and deuterons) at low energies (see table 7) were defined at the half-height of Bragg-like shower curves.

The results of the response and resolution measurements for different structures and gases will be given in tables 2 to 6.

2.3 Summary of errors

The hardware improvements mentioned above have resulted in better experimental accuracies, as compared with ref. [5]. We have accounted for the following sources of error on measured responses, their ratios, and the energy resolutions, which are mainly due to the systematic effects:

- Pedestal spread arising from electronics instabilities. Typical instability of the pedestal position was 2 mip for most of the data (for 0.5 GeV/c pions it was 1.5 mip, and for the 0.3 GeV/c pions and stopping muons with momenta less than 0.75 GeV/c, 1 mip). Since only the front part of the calorimeter (20 planes) was used to measure the electron response, the pedestal instability for electrons was 0.5 mip.
- Pedestal spread due to the U-noise signals, which affects the resolution. The r.m.s. and st. dev. values of the U-noise signals for different calorimeter structures are given later (see table 9). The r.m.s. and the shape of the U-noise distribution depend on the electronics used: for the 'fast' electronics with the smaller differentiation time constant, the distribution is more symmetric, whereas for the 'slow' electronics it has a tail towards higher values.
- The error in response arising from the non-uniformity of the amplification factors was estimated to be $10\%/\sqrt{N_c}$, where N_c is the average number of channels per event with amplitudes above 0. Typical values for 2 GeV/c were: 1.2% for muons; 2% for pions; 3% for electrons.
- Errors in the response of stopping pions and muons (below 1 GeV) due to the uncertainty on the cut used for the separation. These errors amounted to 5–8% for muons and to 2–4% for pions.
- The statistical error in the response and in the resolution for a particular distribution was calculated using the r.m.s. of this distribution. The typical statistics were 4000 events for pions, 2000 events for electrons, 1500 events for muons, and 1000 events for pedestals.
- For 'fast' electronics [5], errors in the response that were due to the LRS 2249A ADC non-linearity amounted typically to:

5% for muon, pion, and proton response;
3% for electron response;
4% for pion/electron ratio;
2% for hadron/muon ratio;
3% for r.m.s. resolution.

All the responses are converted into units of 'mip'. The accuracy of this conversion is 2.5%, as can be derived from the above information.

The error in the resolution depends on several additional factors, such as the definition of resolution (st. dev. or r.m.s.), the calorimeter structure (U-noise shielding), the electronics, etc. Small pile-up effects at beam intensities above 10^4 particles per second were also taken into account. Errors shown in data tables were calculated according to the figures given above.

3. THE CALORIMETER PERFORMANCE WITH DIFFERENT GAS MIXTURES AND STRUCTURES

3.1 The neutron component of a hadronic shower in the U-gas calorimeter

First we review some observations made in ref. [5]:

i) The response of the U-gas sampling calorimeter to pions depends strongly on the gas mixture used. The π/e ratio increases with the increasing content of the hydrogen in the gas mixture, thus making the tuning of π/e possible.

ii) The π/e ratio for the isobutane filling could be further increased by increasing the effective density of the absorber.

These observations were explained by the high sensitivity of the gas detectors to the neutron component of the hadronic shower. The presence of hydrogen in the gas of the detector causes a rise in the hadron response owing to elastic neutron-proton collisions. These collisions are rather rare: the probability of a 1 MeV neutron interaction with hydrogen in isobutane at NTP is about 0.001/cm. However, the amount of ionization deposited in the gas by the recoil proton is, on an average, about 100 times more than that deposited by a minimum-ionizing particle.

The 1 MeV neutrons produced by fast hadrons in nuclear spallation or by low-energy neutrons in (n,f), (n,2n), and (n,3n) reactions will drift inside the calorimeter volume, crossing the detector gaps until either they are captured or they leak out. The number of these neutron crossings depends on the calorimeter structure but is virtually independent of the gas used in the chambers. The detected contribution ΔR_n to the calorimeter response due to neutron interactions with the detector material is, on an average,

$$\Delta R_n/\text{GeV} = N \times W \times A \,,$$

where

N is the number of neutron crossings per GeV of initial hadron energy;
W is the probability of neutron interaction with detector material per crossing;
A is the average detector response per neutron interaction with detector material.

Different gases have different values for W and A. This results in a different contribution of the neutron component to the hadronic response. If the calorimeter structure is varied, then the number of crossings, the probability of interaction, and the detector response to neutron interaction will also vary owing to the variation in the leakage and in the energy spectrum of the neutrons.

The difference between the pion response for the Ar (80%) + CO_2 (20%) and that for the isobutane is clearly seen in fig. 3, where the amplitude distributions for these two gases are shown for a single chamber plane. The number of large amplitudes is higher for isobutane owing to the interaction of the neutrons with the hydrogen in the gas. These rare and rather large amplitudes are called 'spikes'. The tail of large amplitudes for Ar + CO_2 is, we believe, due to the fluctuations in the ordinary component of the hadronic shower. The amplitude distribution for isobutane consists of both the neutron component and the ordinary (non-neutron) hadronic shower component. We assume that the latter is the same as the distribution for Ar + CO_2, which is almost insensitive to the neutron component. Thus the isobutane response spectrum contains the convolution of the Ar + CO_2 spectrum with the neutron spike spectrum.

Therefore, for every calorimeter cell (as well as for every chamber plane or for the whole calorimeter), we can write

$$S_{\mathrm{iso}\,(a)} = \int_0^a S_{\mathrm{Ar}(x)}\, S_{\mathrm{spike}(a-x)}\, dx ,$$

where $S_{\mathrm{iso}(a)}$ is the isobutane spectrum of amplitudes (a);

$S_{\mathrm{Ar}(a)}$ is the Ar + CO_2 spectrum;

$S_{\mathrm{spike}(a)}$ is the unknown 'spectrum of spikes'.

The 'spectrum of spikes' is a statistical combination of single overlapping spikes described by the following parameters:

N_{spike}: the mean number of spikes (it is, in fact, the mean value of the Poisson distribution that determines the normalization of the spike spectrum);

A_{spike}: the mean amplitude of the spikes (since the single-spike spectrum is assumed to have exponential shape, $1/A_{\mathrm{spike}}$ is the slope of the exponent);

r: correlation coefficient between the spike (i.e. neutron) component and the regular Ar + CO_2 component.

The numerical solution of the above integral equation was performed by a Monte Carlo method in order to take into account the statistical nature of the spikes, including correlations between the ordinary and the neutron components. The procedure consisted essentially of making a Monte Carlo calculation of the right-hand side of the above integral equation, and comparing the result with the measured isobutane spectrum. By varying the spike spectrum parameters, we found the minimum of the corresponding χ^2 value, and thus obtained, for every calorimeter cell, the two independent parameters*) that describe the spike spectrum. The mean values of these parameters are shown in fig. 4 as a function of the beam momentum. The parameter A_{spike} is momentum-independent. The parameter N_{spike} rises almost linearly with momentum. This kind of dependence is the expected behaviour of the neutron-component contribution.

In fig. 5 the transverse and longitudinal distributions of spikes N_{spike} are shown. The histograms are the N_{spike} distributions for 6 GeV/c, and the dashed curves are the measured hadronic shower distributions at 6 GeV/c for Ar + CO_2 (ordinary hadronic shower component). Whilst the distribution of the spikes follows closely the longitudinal hadronic shower profile, it is much wider in the lateral direction, suggesting considerable side leakage of neutrons. The lateral leakage occurs because of the anisotropy of the calorimeter structure (or low 'linear density'), the neutron mean free path being longer by a factor of 3 to 4 in the lateral direction than in the longitudinal one.

The correlation coefficient between the total calorimeter response with Ar + CO_2 filling and the total energy of spikes in an event was found as a result of the three-parameter solution of the above

---

*) The third parameter is only meaningful when the above integral equation has to be solved for the whole calorimeter.

integral equation for the whole calorimeter. The correlation coefficient was found to be positive and equal to

$$r = +0.13 \pm 0.04 \ (\chi^2 = 1.0 \text{ per degree of freedom}).$$

Other parameters A_{spike} and $N_{spike(tot)}$ are consistent with those shown in fig. 4. The quality of this solution describing the measured isobutane spectrum is illustrated by fig. 6.

3.1.1 The response of non-hydrogenous gases to the neutron component of a hadronic shower

As was shown in ref. [5], the gases containing hydrogen are very sensitive to the neutron component of the hadronic shower in U-gas sampling calorimeters. Owing to the presence of light nuclei, the non-hydrogenous gases can also be sensitive to neutrons, provided the space-charge effects in proportional gas amplification are not too severe.

We studied two Ar + CO_2 gas mixtures with a different CO_2 content: 20% and 90% (partial pressure). The results are summarized in table 2 and in fig. 7. The fast electronics was used with calorimeter structure 4. The errors due to ADC non-linearity are not included in the errors shown in fig. 7 because they were not important for the comparison of results obtained for the same incident particles at the same energy. It can be seen that the electron and muon responses (normalized to 2 GeV/c muon response) coincide within experimental errors, whilst the pion responses are slightly different. It was found experimentally that

$$e(10 + 90)\%/e(80 + 20)\% = 1.02 \pm 0.01 \,,$$
$$\pi(10 + 90)\%/\pi(80 + 20)\% = 1.14 \pm 0.02 \,.$$

From simple Monte Carlo calculations where only elastic scattering of neutrons is included—and not the space-charge saturation effects in the gas—the above pion ratio is expected to be 1.07.

Thus we conclude that gases with an admixture of light nuclei, such as carbon or oxygen, are weakly sensitive to the neutron component of the hadronic shower. This effect can be used for the fine tuning of the π/e ratio in the U-gas sampling calorimeters. [However, the Ar (10%) + CO_2 (90%) mixture is known to be much slower and requires a higher operating voltage than that needed by the Ar (80%) + CO_2 (20%) mixture.]

3.1.2 Linear density variations

Reference [5] has shown that the hadronic response due to the neutron component increases when the 'linear density' of the uranium absorber is increased. Two structures without Cu shielding were studied [5]:

i) 4.5 mm U + chamber, the structure period 18 mm, with a U linear density of 4.6 g/cm^3;
ii) 9.0 mm U + chamber, the structure period 20 mm, with a U linear density of 8.26 g/cm^3.

To extend the range of linear density variations, we made a scan of the longitudinal shower development inside the uranium with a single chamber and for two linear densities of U absorber, 13.7 g/cm^3 and 4.6 g/cm^3. This was done by arranging 4.5 mm U plates into regular structures with periods 6 and 18 mm, respectively. The scan was made with a single chamber filled either with an Ar (80%) + CO_2 (20%) mixture or with isobutane, which was placed successively behind every absorber for the first 20 absorbers and behind every second absorber for the remaining 76 absorbers.

We found that the electron response (i.e. the integral of the longitudinal shower profile) depended neither on the linear density nor on the gas mixture, whilst the pion response for isobutane was considerably enhanced by the increasing linear density of the absorber.

The results are summarized in table 3 (normalized to a single absorber scanning step). The errors include the systematic and statistical uncertainties. The π/e ratios calculated from table 3, together with the full calorimeter data from table 4 and from ref. [5], are shown in fig. 8 versus the linear density of the U absorber in the structure. The 'full calorimeter' points and the 'single-chamber scan' points are close to each other, suggesting that the amount of chamber material, such as brass, Mylar, etc. (table 1), does not make a significant contribution to the π/e ratio. For isobutane, the π/e ratio increases dramatically with the increase of the U absorber linear density. The reason for this effect is the better neutron containment in the calorimeter volume at the higher density. At low linear density ($\sim$ 4.5 g/cm^3), according to neutron-transport Monte Carlo calculations [7], about 80% of the neutrons leak out of the calorimeter (mainly in the lateral direction). When the neutron containment improves, the neutrons have more chance to cross the detector planes and the response increases accordingly. Of course, for a calorimeter of infinite size where no neutron leakage occurs, there should be no response variation with linear density, and the π/e ratio should reach a value of approximately 4 for the isobutane, thus showing strong 'overcompensation' due to the neutron component of the hadronic shower. However, for the structures used in the present study, the neutron leakage effect was still important and had to be accounted for in the comparison of different absorber structures.

For the Ar (80%) + CO_2 (20%) mixture, a small increase in the π/e ratio was also observed (fig. 8). This increase cannot be explained by the neutron component alone (the contribution due to the neutron interaction with carbon and oxygen is far too small for that), but might be due to better shower containment in the more dense structures.

The solid curve in fig. 8 is the result of a simple neutron-transport Monte Carlo program that simulates nuclear reactions in the energy range 0–20 MeV for the calorimeter structures. It uses the neutron spallation energy spectrum [8] and calculates the response of the detector to neutron interactions in the gas. This simulated neutron contribution with appropriate normalization is shown in fig. 8 as the difference between the isobutane and the Ar + CO_2 data. The dashed curve for the Ar + CO_2 points is drawn to guide the eye.

3.1.3 Neutron component moderation by material containing hydrogen

The probability of neutron interaction with gases in a U-gas sampling calorimeter is very low ($\lesssim 10^{-3}$). Therefore, neither the number of chamber crossings made by neutrons, nor their energy spectra, is affected by the chamber gas. However, if the amount of hydrogen-containing material in the calorimeter is large, i.e. the probability of interaction with hydrogen per crossing is close to unity, then the number of neutron crossings and the neutron spectra are modified. To study this effect, we used a structure where the chambers were shielded by 2 mm Plexiglas sheets on either side (structure No. 2 in table 1). The corresponding data are given in table 5.

The responses to electrons and pions for the two U structures with different shielding material are shown in fig. 9 for the isobutane filling. The replacement of 1 mm Cu sheets by 2 mm Plexiglas sheets increases the electron response and decreases the response to pions. The increase of the electron response is due partly to sampling variation — since the energy loss in 1 mm Cu is higher than in 2 mm Plexiglas — and partly to the transition effect of electromagnetic shower propagation in the layers of absorber with different Z [9]. Both effects can be seen in fig. 10, where the results of measurements of the electron response (in mip) for different absorber-shielding structures are given. The horizontal axis is ΔE_{mip}, i.e. the energy loss of a minimum-ionizing particle in one absorber layer. The points are the weighted average of several measurements with different gases. The curve shown in this figure is the $1/\Delta E_{mip}$ dependence plotted through the extreme points. The transition effect results in a deviation from the $1/\Delta E_{mip}$ dependence in this figure. The effect seen for the Cu shield agrees qualitatively with calculations made in ref. [9].

The responses to pions for Ar (80%) + CO_2 (20%) and isobutane, and for different absorber-shielding structures (the density of the U absorber was kept constant), are shown in fig. 11 versus ΔE_{mip}. The points for the Ar + CO_2 mixture follow approximately the $1/\Delta E_{mip}$ dependence as shown by a curve plotted through the extreme left point. The difference in response between isobutane and Ar + CO_2 is almost the same for structures with no shielding and for those with 1 mm of Cu, but essentially it is reduced for the structure with 2 mm Plexiglas shielding. This effect is due to the moderation of the neutron component in the structure containing hydrogen, as can be concluded by comparing the measured values with the results of the Monte Carlo simulation (shown as 'diamonds' in fig. 11) of the neutron contribution, i.e. the difference between isobutane and Ar + CO_2 responses. The normalization of Monte Carlo data is the same as in fig. 8.

3.2 The calorimeter response at low energies

The calorimeter responses to electrons, muons, pions, protons, and deuterons in the momentum range 0.3–3 GeV/c for structure No. 3 are given in tables 6a–d. The pion–muon separation for a beam momentum of 0.5 GeV/c is shown in fig. 12.

The responses for different incident particles are shown in figs. 13 versus kinetic energy: a) for the Ar (80%) + CO_2 (20%) mixture, and b) for the isobutane filling. The electron and positron responses are linear and, within errors, the same for both gases. Muons with kinetic energy below approximately 1.1 GeV are stopped in the calorimeter. In fig. 13 the responses to muons of higher energies are plotted versus the calculated energy deposit in the calorimeter. The muon responses are linear within experimental errors and are equal for both gases and both beam polarities. At the same kinetic energy, the muon response is higher than the electron one. We believe this is due to 'migration and transition effects', discussed in refs. [9–11].

The hadronic response becomes non-linear at kinetic energies below 2 GeV. For the Ar + CO_2 mixture, which is almost insensitive to neutrons, the protons and deuterons with the same kinetic energy give a response that is close to that of a pion; the pion response, which was lower than that of the electron at $E_{kin} > 1$ GeV, increases, and at $E_{kin} \approx 0.8$ GeV it becomes equal to the electron response and then, at still lower energies, approaches the response of muons. This effect was experimentally observed and explained in ref. [12] for calorimeters with other absorber and readout structures. At lower kinetic energies, hadrons, like muons, lose their energy through ionization. Therefore the relative contribution of ionization to the energy loss becomes larger and the hadron response increases to the value of the muon response. In fig. 14 the averaged longitudinal shower development profiles are shown for proton momenta of 2.08 and 1.04 GeV/c for Ar + CO_2 gas. It is clear that protons of 1.04 GeV/c look like stopping particles, whilst 2.08 GeV/c protons have a smoothly falling shower curve. The measured ranges of muons, protons, and deuterons are given in table 7, together with the results of dE/dx calculations [13], which agree well with the measurements.

The hadron response for the isobutane filling (fig. 13b) is higher than that for Ar + CO_2. It was also higher than the electron response in the whole energy range. The hadron response approaches that of muons at energies lower than those for the Ar + CO_2 mixture, in spite of the relative increase in the ionization contribution, which makes the hadrons look like stopping particles for both gases equally.

The electron/hadron and electron/muon response ratios at the same kinetic energy, versus the kinetic energy of the incident particles, are shown in fig. 15 for the Ar (80%) + CO_2 (20%) mixture, and in fig. 16 for isobutane. The average ratio of electron/muon responses for two gases is 0.65 ± 0.04 (calorimeter structure No. 3). At energies above 2 GeV, the electron/hadron ratio is almost energy-independent, but it is different for isobutane and the Ar + CO_2 chamber filling. At lower energies, the electron/hadron ratio becomes energy-dependent. For Ar + CO_2 it reaches the value of the electron/muon at $E_{kin} \approx 0.2$ GeV for all types of particles. For isobutane, this happens at somewhat lower energies.

3.3 The energy resolution

3.3.1 The energy resolution for electrons, pions, and stopping muons with the Ar (80%) + CO_2 (20%) mixture

The energy resolution for electrons, and for the low-energy muons stopped in the calorimeter, is shown in fig. 17a as a function of the kinetic energy of the incident particles for calorimeter structure No. 3. The resolution in this figure is the standard deviation (SD) parameter of the Gaussian fit to the corresponding amplitude distributions, combining the first 20 chamber planes for electrons and all 86 planes for muons. The U-noise contribution to the width is about a factor of 2 smaller for electrons than for muons (20 chambers against 86 chambers). This contribution is not subtracted in fig. 17a. The lines there correspond to the resolution dependence

$$33.5\%/\sqrt{E_{kin}(\mathrm{GeV})} \text{ for electrons ,}$$

$$28.5\%/\sqrt{E_{kin}(\mathrm{GeV})} \text{ for muons .}$$

Because of U-noise pile-up, the pedestal distribution is not symmetric. Therefore the resolution was corrected for by subtracting the dispersion (r.m.s. squared) of the pedestal distribution from the dispersion of the electron and muon distributions. The corresponding results are shown in fig. 17b. The straight lines on the figure correspond to

$$33.5\%/\sqrt{E_{kin}(\mathrm{GeV})} \text{ for electrons ,}$$

$$22.0\%/\sqrt{E_{kin}(\mathrm{GeV})} \text{ for muons .}$$

The electron resolution is almost the same as the Gaussian one shown in fig. 17a. The muon resolution is better than that for electrons because the muon response is larger than the electron one and the track-length fluctuations for muons are considerably smaller.

The amplitude distribution for pions, with an Ar + CO_2 mixture, looks almost Gaussian. An example of 6 GeV/c pion distribution is shown in fig. 18. The r.m.s. resolution for this distribution is (33 ± 2)%, whilst the standard deviation of the fitted Gaussian (also shown in fig. 18) gives (29 ± 2)%. The right-hand-side tail comes from the interactions of neutrons with the light nuclei and from the U noise and accidental beam-particle pile-ups. The relative U-noise contribution to the r.m.s. of the distributions becomes larger at smaller energies. However, the resolution, defined as the Gaussian st. dev., is virtually unaffected by the U noise, as was seen above in the case of electrons.

Since the hadron response below 1.5 GeV is not linear (fig. 19a), in fig. 19b we plot the st. dev. of the Gaussian fit to the measured amplitude distributions (in mip) divided by $\sqrt{E_{kin}}$ as a function of the kinetic energy for pions and protons. The U noise is not subtracted here, and the response is determined as the total sum of the amplitudes of the 86 chamber planes (structure No. 3). The st. dev. values for pions and protons are almost the same, and behave as $C\sqrt{E_{kin}(\mathrm{GeV})}$ (where C is a constant) in the whole energy range, except for the lowest energy point where U noise starts to contribute. This constant, averaged over energies of 0.4–0.6 GeV, is equal to (27.2 ± 2.5) mip. If the energy response were linear, then in order to convert the st. dev. mip value into the conventional relative resolution (in %), we would have to divide it by the mean hadronic response (shown in fig. 19a). The st. dev. muon resolution is also shown in fig. 19b for comparison. The corresponding r.m.s. resolutions for pions, protons, and muons have been given in tables 6; typical U-noise r.m.s. are listed later in table 9.

3.3.2 An off-line method of resolution improvement

The idea of this method is the following. Information about the incident hadron energy is contained not only in the total sum of the calorimeter amplitudes but also, generally speaking, in every amplitude measured in the calorimeter. In practice, we used the total calorimeter response (S0) and the five highest amplitudes (S1–S5) in each event, and summed them up according to the least-squares method (LSM) [14]. In fig. 20 the mean values of the three highest amplitudes ⟨S1⟩, ⟨S2⟩, and ⟨S3⟩ are shown for isobutane as a function of the incident momentum. To apply the LSM, it is necessary to find, from calibration measurements, the mean values ⟨S0⟩, ..., ⟨S5⟩ and the elements of the corresponding covariance matrix R_{ij} (i, j = 0, ..., 5) as functions of the incident energy. Then, according to the LSM, for each event with the measured total response S0 and the five highest amplitudes S1, ..., S5, the energy E can be determined by minimization of the function F:

$$F(E) = \sum_{i,j=0}^{5} [S_i - \langle S_i \rangle (E)] \cdot R_{ij}^{-1}(S0) \cdot [S_j - \langle S_j \rangle (E)] \; .$$

In fig. 21 the response to 4.6 GeV/c pions is shown for both Ar (80%) + CO_2 (20%) and isobutane. The dashed lines are the initial distributions and the solid lines are the LSM reconstructed distributions for the same experimental data. The LSM does not change the mean values of the distributions, but makes them symmetric by removing the tails and improves the resolution. The r.m.s. resolution as a function of the pion kinetic energy is shown in fig. 22 in the energy range 1–6 GeV for the Ar (80%) + CO_2 (20%) mixture and for isobutane, before and after the application of the LSM. There is a greater improvement for isobutane than for Ar + CO_2. The procedure brings the isobutane resolution closer to the resolution of Ar + CO_2. For Ar + CO_2, the r.m.s. resolution reconstructed by the LSM almost coincides with the st. dev. value.

3.3.3 The double-chamber structure

We have performed a dedicated test made with 9 mm U absorbers shielded on both sides by 1 mm Cu sheets and interleaved with double-chamber layers (structure No. 5), the wires of these chambers being aligned. The odd and the even chambers were connected to two separate gas-supply systems; thus they could work independently with either the Ar (80%) + CO_2 (20%) mixture or isobutane. With this arrangement we obtained two calorimeters built into one another (intercalated), and were able to measure the same hadron shower event simultaneously for two different gases.

Because the Ar + CO_2 mixture is not sensitive to neutrons, the chambers filled with this mixture measure the regular shower component. Chambers filled with isobutane are sensitive to the regular component as well as to the neutron component of the hadronic shower. Thus in the same event it was possible to measure both the regular and the neutron component and to study the correlation between them. In subsection 3.1 we have determined the correlation coefficient between regular and neutron components at a statistical level through a comparison of the total response distributions for the isobutane and the Ar + CO_2. With the double-chamber structure, the coefficient was found from the comparison of measured response–response correlations for the two intercalated calorimeters. Two methods of extracting the correlation coefficient were used, but as both gave similar results, only one of them—the Monte Carlo procedure—is described here. Using this method we started with the (Ar + CO_2) + (Ar + CO_2) experimental data, where one set of Ar + CO_2 data was used to simulate the isobutane calorimeter response. In order to obtain the isobutane response, the parameter of correlation between the Ar + CO_2 calorimeter response and the mean number of neutron spikes simulated statistically in the calorimeter was introduced (the parameters of the spikes have been determined in subsection 3.1). Then the '(Ar + CO_2) + isobutane' correlation plot was simulated and compared with the one measured with the real (Ar + CO_2) + isobutane structure. By performing the corresponding χ^2 minimization, the correlation coefficient between the hadronic shower deposit in Ar + CO_2 and the energy deposited by the neutron component was determined. It was found to be positive and equal to 0.08 ± 0.03 for the energy range 2 to 6 GeV.

The traditional explanation [10, 11, 15] of the compensation mechanism in U calorimeters assumes that there is a negative correlation between the regular visible energy of a hadronic shower and the number of neutrons produced by the shower, i.e. if in a given event the visible energy increases owing to a fluctuation, the number of neutrons produced in the same event should decrease. The positive sign*) of the measured correlation coefficient means that the neutron component does not lead to any compensation of the visible-energy fluctuations, and therefore cannot improve the energy resolution of U gas calorimeters.

As the response–response correlation between the two intercalated calorimeters is not large, the energy resolution for the sum of odd + even chambers is better than for only odd or only even chambers. This is illustrated in fig. 23, where the calorimeter response to 2 GeV/c pions is shown for odd planes and for odd + even planes. No cuts are applied to the data. The latter distribution has somewhat better resolution; however, it also has a tail due to U noise and to rather rare neutron spikes.

The spikes can be efficiently suppressed in the double-chamber structure by rejecting events for which the difference between signals in two adjacent cells exceeds some threshold. The corresponding response (threshold of 25 mip) for 2 GeV/c pions is shown in fig. 24 together with a Gaussian fit. The tail is essentially reduced, and the response looks almost Gaussian. This rejection procedure works even more efficiently for the gas mixture (Ar + CO_2) + isobutane and when the gas filling is isobutane + isobutane.

In fig. 25 the absolute r.m.s. resolution for the double-chamber structure, divided by the square root of the kinetic energy of the pion, is shown as a function of beam momentum for two gas combinations. The energy resolution of 9 mm U absorber + copper shield + double-chamber structure, with any combination of gas filling and with the spike rejection procedure applied, is very close to the resolution of the calorimeter with 4.5 mm U absorber + single-chamber structure and with the Ar + CO_2 mixture.

The spike rejection also affects the mean value of the hadronic response. The pion responses versus beam momentum for two gas combinations, before and after the application of the spike rejection procedure, are shown in fig. 26 together with the electron response, which is also slightly affected by this procedure. By varying the rejection threshold, some tuning of the hadronic response can be made.

4. OTHER CALORIMETER STUDIES

4.1 The U-gas calorimeter performance in a magnetic field

In the L3 detector the calorimeter operates in the magnetic field, and we should know how the field affects its performance. In order to simulate the L3 magnetic field environment, a dipole magnet with a 60 cm gap was used at the ITEP PS. Only the electromagnetic section of the U-gas calorimeter test module, with 16 absorbers (500 × 500 × 4.5 mm^3) and 17 chamber planes (structure

---

*) A possible explanation of this is that the protons of 10–100 MeV, whose contribution to the visible energy is positively correlated with the neutron one, dominate the hadron response.

No. 6 in table 1), was installed in the magnet. The signal wires were parallel to the magnetic field for the odd chamber planes and perpendicular to the field for the even ones. Thus in the magnetic field the orientation of the wires was exactly as in the L3 detector. The non-uniformity of the field was below 3% inside the calorimeter test module.

The 1–6 GeV energy scan for this set-up was made with muons and electrons at magnetic fields of 0, +0.5, −0.5, and −0.7 T. The pedestal distributions were not affected by the field. No response or resolution dependence on the polarity of the magnetic field was observed. The results of the response and resolution measurements are summarized in table 8 together with the results of corresponding EGS4 [16] Monte Carlo calculations. No essential dependence of the response (in mip) on the magnetic field was observed for electrons. The only effect of the magnetic field on the electron response distributions is the appearance of a small tail on the right-hand side of the distribution owing to spiralling of low-energy electrons from the electromagnetic shower. The electron resolution, defined as a Gaussian standard deviation, is almost insensitive to this tail, but the effect is more pronounced in the r.m.s. resolution of the odd chamber planes (fig. 27) where the wires are directed parallel to the magnetic field. We believe that the pion response and the resolution are even less affected by the magnetic field.

4.2 The calorimeter response to muons

The muon response in the U sampling calorimeter is strongly energy-dependent, because of δ electrons.

The response of the single chamber plane to muons was measured in two positions: in front of the U absorber, and behind the 4.5 cm of U. The ^{55}Fe source was installed behind a thin window made in one of the tubes of a chamber. Thus the measured muon deposit in the chamber was calibrated in keV. In fig. 28 the muon response for the chamber positions, both outside and inside the absorber, is shown as a function of the beam momentum. The muons were selected by the U and the muon filter behind the chamber (6 abs. lengths in total). The response of the chamber situated behind the U block is higher and rises with energy owing to δ electrons created in the U and detected by the chamber. The contribution of muon radiation losses [13] is negligibly small at these energies, as compared with the observed effect. The accuracy of intercalibration for these two curves is better than ±3%. The absolute energy calibration accuracy (vertical scale) is ±5% and is determined mainly by space-charge effects in the gas mixture Ar (80%) + CO_2 (20%).

4.3 The U-noise and electronics optimization

The U noise is an important characteristic of U calorimeters. It worsens the resolution at low energies, and produces large spurious signals that can influence the energy trigger. On the other hand, it provides a convenient way of carrying out the global calorimeter calibration [6]. We have performed a detailed U-noise study for our calorimeter.

In the absence of coherent electronics noise, the statistically distributed U noise, which produces the signal only in one proportional tube, will contribute to the r.m.s. of the pedestal distribution proportionally to the square root of the number of hits for a given electronics channel. This means that the dispersion of the pedestal distribution is proportional to the gate width of the readout electronics and to the total surface area of the chambers. Shielding material between the U and the chamber changes the U-noise counting rate and U-noise signal spectrum. The bandwidth of electronics and electron drift velocity in the proportional tube can affect the U-noise signals as well as the response to shower particles, which is due to different fractions of the collected charge falling inside the gate.

Our 'slow' Sample-and-Hold electronics had 2 μs effective gate width, and the 'fast' electronics usually operated [with the Ar (80%) + CO_2 (20%) mixture] with a gate width of 300 ns. The differentiation time constant of the 'fast' electronics (~ 500 ns) resulted in a pedestal distribution that was more symmetric than that for the 'slow' electronics. In table 9 the Gaussian st. dev. and r.m.s. of pedestal distributions with and without the 1 mm Cu shielding are given for the two versions of readout electronics. The data shown in the table are for 56 chambers, with the total surface area being approximately equal to that of a hadron calorimeter module in the L3 detector.

The optimization of the fast-electronics gate width was made through a scan in the range 100–1000 ns. The results are shown in fig. 29. The minimum of U-noise r.m.s. is around 300 ns, whilst the optimum for electron resolution lies somewhat higher. The π/e ratio does not change over the whole range of the gate width. In fig. 30, the pedestal distribution for 56 chambers (structure No. 4) is shown for a 300 ns gate width (fast-electronics readout). We can conclude that in the absence of coherent noise, the r.m.s. of one calorimeter module of the L3 detector should be about (210 ± 20) MeV (electron response equivalent).

5. CONCLUSION

Further confirmation of the importance of the neutron component contribution to the detected signal in U–gas sampling hadron calorimeters was obtained. The neutrons produced in the hadronic shower propagate in the U absorber in a different way than the other shower particles. Therefore, in calorimeters with detectors that are sensitive to neutrons, the response can depend considerably on neutron leakages.

The hydrogen contained in both active (detector gas) and passive (e.g. shielding plates) material affects the hadronic response significantly. This feature can be used for the tuning of the hadron/electron response ratio.

The correlation between the regular and neutron components of the hadronic shower detected in the U–gas sampling calorimeters was found not to be negative, contrary to naïve expectations. This explains the fact that in the gas calorimeters, the detection of the neutron component does not improve the energy resolution.

The electron/muon response ratio was found from the direct measurements of the responses for electrons and muons that were fully absorbed in the calorimeter. This ratio is equal to 0.65 ± 0.04.

Measured calorimeter response to muons shows rather strong energy dependence due to the enhanced contribution of δ electrons. The natural radioactivity of depleted U results in an accidental 'U noise', which contributes (about 210 MeV, electron signal equivalent) to the calorimeter resolution at low energies. It was shown that the magnetic fields of up to 0.7 T do not affect the calorimeter performance significantly.

Acknowledgements

The authors from the University of Michigan wish to acknowledge the support of the US National Science Foundation.

REFERENCES

[1] A. Arefiev et al., Moscow report ITEP-150 (1983).

[2] F. Celletti et al., Nucl. Instrum. Methods **225** (1984) 493.

[3] B. Bleichert et al., Aachen report PITHA 85/11 (1985).

[4] A. Arefiev et al., Nucl. Instrum. Methods **A245** (1986) 71.

[5] Yu. Galaktionov et al., Nucl. Instrum. Methods **A251** (1986) 258.

[6] S. Burov et al., preprint CERN-EP/88-84 (1988).
A. Arefiev et al., preprint CERN-EP/88-76 (1988).

[7] V. Kazaritsky, Moscow report ITEP 86-61 (1986).

[8] T.W. Armstrong et al., Nucl. Instrum. Methods **222** (1984) 540.

[9] K. Pinkau, Phys. Rev. **B139** (1965) 1548.

[10] H. Brückmann et al., *in* Proc. 15th Winter Meeting on Fundamental Physics, Sevilla, 1987 (World Scientific, Singapore, 1988), p. 69.

[11] R. Wigmans, Nucl. Instrum. Methods **A259** (1987) 389.

[12] T. Åkesson et al., Nucl. Instrum. Methods **A241** (1985) 17.

[13] W. Lohmann et al., CERN 85-03 (1985).
R.M. Sternheimer et al., Atomic Data and Nucl. Data Tables **30** (1984) 261.

[14] See, for example, W. Hamilton, Statistics in physical science (New York, 1964).

[15] C.W. Fabjan et al., Phys. Lett. **60B** (1975) 105.

[16] W.R. Nelson et al., Stanford report SLAC-265 (1985).

Table 1

List of calorimeter structures

No.	Structure	Absorber	Structure period (mm)	Gas Mixture
1	M + 55(A+M) + 30(A+I)	4.5 mm U, no shield	18	isobutane
2	M + 55(A+M) + 30(A+I)	4.5 mm U + 2 × 2 mm Plexiglas	18	Ar (80%) + CO_2 (20%) isobutane
3	M + 55(A+M) + 30(A+I)	4.5 mm U + 2 × 1 mm Cu	18	Ar (80%) + CO_2 (20%) isobutane
4	56(A+M) + 23(A+I)	4.5 mm U + 2 × 1 mm Cu	18	Ar (80%) + CO_2 (20%) Ar (10%) + CO_2 (90%)
5	28(A+2M) + 16(A+2I)	9.0 mm U + 2 × 1 mm Cu	33.64	Ar (80%) + CO_2 (20%) isobutane
6	M + 16 (A+M)	4.5 mm U + 2 × 1 mm Cu	18	Ar (80%) + CO_2 (20%)

Definition of symbols

M ≡ 'M-type' chamber [5]: 0.610 g/cm^2 brass + 0.070 g/cm^2 Mylar + 6 mm gas.

I ≡ 'I-type' chamber [5]: 0.360 g/cm^2 stainless steel + 0.255 g/cm^2 G10 + 4 mm gas.

A ≡ absorber: 4.5 mm of depleted ^{238}U (8.216 g/cm^2)

2 × 1.0 mm of 99.9% pure Cu (1.731 g/cm^2)

2 × 2.0 mm of Plexiglas ($C_5H_8O_2$) (0.472 g/cm^2)

Table 2

Calorimeter response (in mip) and resolution (in %) for structure No. 4, for two Ar + CO$_2$ mixtures: (80 + 20)% and (10 + 90)%; 79 (absorber + chamber) layers; 'fast' electronics

Beam momentum (GeV/c)	Electrons (Gaussian fit) Mean (mip)	Electrons (Gaussian fit) St. dev. (%)	Pions Mean (mip)	Pions r.m.s. (%)	Pions St. dev. (%)	Muons Mean (mip)
Ar (80%) + CO$_2$ (20%) [gate width 300 ns, 1 mip = 9 ADC channels]:						
−6.24	284.0 ± 12.1	13.5 ± 2.2	223.0 ± 12.2	31.0 ± 1.8	29.5 ± 1.7	93.0 ± 5.2
−5.20	246.0 ± 11.5	14.8 ± 2.2	187.0 ± 10.3	34.0 ± 1.8	31.0 ± 1.8	91.5 ± 5.1
−4.16	198.0 ± 8.5	17.3 ± 2.2	146.0 ± 8.2	38.0 ± 1.9	35.0 ± 1.8	88.0 ± 5.0
−3.12	148.0 ± 6.3	19.0 ± 2.3	110.0 ± 6.3	42.0 ± 2.0	41.0 ± 2.0	84.0 ± 4.8
−2.08	99.0 ± 4.3	22.5 ± 2.3	72.0 ± 4.4	51.0 ± 2.2	48.0 ± 2.1	79.0 ± 4.6
−1.04	50.0 ± 2.2	32.0 ± 2.4	40.0 ± 3.0	70.0 ± 2.7	61.0 ± 2.5	
Ar (10%) + CO$_2$ (90%) [gate width 400 ns, 1 mip = 8 ADC channels]:						
−6.24	290.0 ± 12.3	15.1 ± 2.2	254.0 ± 13.9	32.0 ± 1.8	30.0 ± 1.7	97.0 ± 5.4
−5.20	250.0 ± 11.7	16.0 ± 2.2	209.0 ± 11.5	35.5 ± 1.8	32.0 ± 1.8	93.5 ± 5.2
−4.16	203.0 ± 8.7	18.0 ± 2.2	169.0 ± 9.4	40.0 ± 1.9	34.0 ± 1.8	91.0 ± 5.1
−3.12	152.0 ± 6.5	21.0 ± 2.3	125.0 ± 7.1	46.0 ± 2.1	42.2 ± 2.0	84.0 ± 4.8
−2.08	100.0 ± 4.3	25.5 ± 2.3	83.0 ± 4.9	55.0 ± 2.3	47.1 ± 2.1	79.0 ± 4.6
−1.04	52.0 ± 2.3	37.0 ± 2.5	47.5 ± 3.3	71.0 ± 2.7	59.0 ± 2.4	
+1.04	51.5 ± 2.3	33.0 ± 2.4	48.0 ± 3.3		65.0 ± 2.5	
+2.08	100.0 ± 4.3	22.5 ± 2.3	84.0 ± 5.0		52.0 ± 2.2	79.0 ± 4.6

Table 3

The calorimeter response (in mip) to different particles, using the 'chamber scan' method; no shield; slow electronics

Gas mixture	Beam momentum (GeV/c)	Calorimeter density (g/cm^3)				
		4.6			13.7	
		Electrons	Pions	Protons	Electrons	Pions
Ar (80%) + CO$_2$ (20%)	+2.08	142.0 ± 3.6	107.4 ± 2.8	76.8 ± 1.6		
	+1.04	69.0 ± 1.6	68.8 ± 2.0	38.4 ± 1.2		
	−2.08	143.2 ± 3.6	108.0 ± 2.8		133.2 ± 2.8	120.2 ± 2.6
Pure isobutane	−2.08	140.0 ± 3.2	196.0 ± 4.6		142.0 ± 3.0	488.0 ± 10.6

Table 4

Calorimeter response (in mip) and resolution (in %) for structure No. 1, for isobutane; 'no shield'; slow electronics.

Beam momentum (GeV/c)	Electrons (Gaussian fit)		Pions		Muons
	Mean (mip)	St. dev. (%)	Mean (mip)	r.m.s. (%)	Mean (mip)
−3.12	212.0 ± 6.5	19.5 ± 2.2	263.0 ± 5.9	57.0 ± 1.6	87
−2.08	140.0 ± 4.4	24.5 ± 2.2	177.0 ± 4.3	68.3 ± 1.7	86
−1.04	70.0 ± 2.3	33.2 ± 2.3*)	97.0 ± 3.6	84.0 ± 2.4*)	

*) Pedestals r.m.s. (U noise) subtracted.

Table 5

Calorimeter response (in mip) and resolution (in %)
for structure No. 2; 2 mm Plexiglas shield; slow electronics

Beam momentum	Electrons (Gaussian fit)		Pions		Muons
(GeV/c)	Mean (mip)	St. dev. (%)	Mean (mip)	r.m.s. (%)	Mean (mip)
Ar (80%) + CO_2 (20%):					
−3.12	185.0 ± 5.7	19.0 ± 2.2	128.0 ± 3.4	55.0 ± 1.6	91.0 ± 2.4
				48.0 ± 1.6*)	
−2.08	128.0 ± 4.0	24.1 ± 2.2	87.0 ± 2.8	65.0 ± 1.7	86.0 ± 2.4
				51.0 ± 1.6*)	
−1.04	64.0 ± 2.1	34.1 ± 2.3*)	49.0 ± 2.5	79.0 ± 2.4	66.0 ± 4.0
				64.0 ± 2.3*)	
			45.0 ± 2.7	90.0 ± 3.0	
				74.0 ± 2.9*)	
Isobutane:					
−3.12	193.0 ± 5.9	20.0 ± 2.2	200.0 ± 4.7	60.5 ± 1.6	
−2.08	129.0 ± 4.0	23.5 ± 2.2	133.0 ± 3.5	72.0 ± 1.6	86.0 ± 2.4
−0.99	59.0 ± 2.0	37.0 ± 2.3*)	60.0 ± 3.1	108.0 ± 3.0	58.0 ± 3.5
			60.0 ± 3.2	109.0 ± 3.0	
−0.52	30.0 ± 1.1	49.0 ± 2.5*)	36.0 ± 2.2	122.0 ± 3.3	33.0 ± 2.5

*) Pedestals r.m.s. (U noise) subtracted.

Tables 6a–d

Calorimeter response (in mip) and resolution (in %) for structure No. 3 with 1 mm Cu shield; slow electronics

Table 6a

Gas mixture Ar (80%) + CO_2 (20%); negative beam

Beam momentum (GeV/c)	Electrons (Gaussian fit)		Pions		Muons	
	Mean (mip)	St. dev. (%)	Mean (mip)	r.m.s. (%)	Mean (mip)	r.m.s. (%)
−2.08	105.0 ± 3.3	24.0 ± 2.2	82.0 ± 2.7	50.0 ± 1.6 42.1 ± 1.6*)	91.3 ± 2.4	33.0 ± 1.2 22.0 ± 1.1*)
−1.04	54.5 ± 1.8	32.5 ± 2.3	44.0 ± 2.5	70.5 ± 2.3 60.0 ± 2.3*)	70.8 ± 4.2	31.6 ± 3.8 26.3 ± 3.8*)
−0.78	40.0 ± 1.4	37.0 ± 2.3	36.0 ± 2.5	76.0 ± 2.9 61.9 ± 2.9*)	49.8 ± 3.1	41.6 ± 4.2 29.5 ± 4.1*)
−0.52	25.0 ± 1.0	46.5 ± 2.4 46.0 ± 2.4*)	24.0 ± 1.9	94.0 ± 3.3 70.0 ± 3.2*)	32.2 ± 2.4	51.5 ± 4.9 33.2 ± 4.9*)
−0.312	15.0 ± 0.8	61.4 ± 2.7 56.0 ± 2.7*)	14.5 ± 1.3	138.0 ± 4.5 88.3 ± 4.2*)	16.7 ± 1.7	76.6 ± 6.0 43.1 ± 5.9*)

*) Pedestals r.m.s. (U noise) subtracted.

Table 6b

Gas mixture Ar (80%) + CO_2 (20%); positive beam

Beam momentum	Electrons (Gaussian fit)		Pions		Muons		Protons	
(GeV/c)	Mean (mip)	St. dev. (%)	Mean (mip)	r.m.s. (%)	Mean (mip)	r.m.s. (%)	Mean (mip)	r.m.s. (%)
+3.12	156.0 ± 4.8	18.5 ± 2.2	124.0 ± 3.3	50.0 ± 1.6 41.0 ± 1.5$^{*)}$	93.0 ± 2.4		97.0 ± 3.0	59.0 ± 1.7 43.0 ± 1.6$^{*)}$
+2.08	104.0 ± 3.3	23.0 ± 2.2	83.0 ± 2.7	52.0 ± 1.6 50.0 ± 1.6$^{*)}$	87.2 ± 2.4	32.5 ± 1.2 21.7 ± 1.1$^{*)}$	57.5 ± 2.5	67.0 ± 1.8 56.0 ± 1.8$^{*)}$
+1.04	52.5 ± 1.8	32.0 ± 2.3	43.5 ± 2.4	74.0 ± 2.3 64.0 ± 2.3$^{*)}$	65.0 ± 4.0	43.7 ± 3.8 25.1 ± 3.8$^{*)}$	28.5 ± 1.8	82.0 ± 2.2 64.0 ± 2.1$^{*)}$
+0.78	40.1 ± 1.4	38.0 ± 2.3	35.0 ± 2.5	80.0 ± 2.9 76.0 ± 2.9$^{*)}$	49.6 ± 3.0	44.8 ± 4.2 30.2 ± 4.1$^{*)}$	19.2 ± 1.7	123.0 ± 2.9 87.0 ± 2.7$^{*)}$
+0.52	25.0 ± 1.0	50.0 ± 2.5 48.0 ± 2.4$^{*)}$	24.8 ± 1.9	94.0 ± 3.2 80.0 ± 3.2$^{*)}$	31.1 ± 2.3	36.7 ± 4.9$^{*)}$		
+0.312	14.2 ± 0.7	74.0 ± 2.9 64.0 ± 2.8$^{*)}$	14.9 ± 1.3	136.0 ± 4.4 99.9 ± 4.2$^{*)}$	17.4 ± 1.7	39.4 ± 5.8$^{*)}$		
Deuteron 2.08 GeV/c: mean = (40.1 ± 2.5) mip; r.m.s. = (86 ± 5)%								

*) Pedestals r.m.s. (U noise) subtracted.

Table 6c

Isobutane; negative beam

Beam momentum	Electrons (Gaussian fit)		Pions		Muons	
(GeV/c)	Mean (mip)	St. dev. (%)	Mean (mip)	r.m.s. (%)	Mean (mip)	r.m.s. (%)
− 2.08	100.0 ± 3.1	21.5 ± 2.2	158.0 ± 3.9	66.0 ± 1.6	91.0 ± 2.4	29.3 ± 1.2 23.6 ± 1.1*)
− 1.04	50.0 ± 1.7	31.5 ± 2.3	73.0 ± 3.0	83.0 ± 2.3	70.6 ± 4.2	35.2 ± 3.8 29.7 ± 3.8*)
− 0.78	38.0 ± 1.3	37.0 ± 2.3	64.0 ± 3.2	96.0 ± 2.9 93.0 ± 2.8*)	52.9 ± 3.2	42.7 ± 4.2 35.7 ± 4.1*)
− 0.52	25.0 ± 1.0	49.0 ± 2.4 45.0 ± 2.4*)	42.0 ± 2.4	113.0 ± 3.1 106.0 ± 3.1*)	33.5 ± 2.5	42.6 ± 4.9*)
− 0.312	14.0 ± 0.7	64.0 ± 2.8 56.0 ± 2.7*)	21.0 ± 1.6	150.0 ± 4.1 129.0 ± 4.0*)	18.1 ± 1.8	54.8 ± 5.8*)

*) Pedestals r.m.s. (U noise) subtracted.

Table 6d
Isobutane; positive beam

Beam momentum (GeV/c)	Electrons (Gaussian fit)		Pions		Muons		Protons	
	Mean (mip)	St. dev. (%)	Mean (mip)	r.m.s. (%)	Mean (mip)	r.m.s. (%)	Mean (mip)	r.m.s. (%)
+2.08	104.0 ± 3.3	22.5 ± 2.2	161.0 ± 4.0	65.0 ± 1.6	92.5 ± 2.4	32.5 ± 1.2 22.3 ± 1.1$^{*)}$	118.5 ± 3.4	67.0 ± 1.7
+1.04	51.2 ± 1.7	32.0 ± 2.3	75.0 ± 3.1	81.0 ± 2.3	70.4 ± 4.2	43.3 ± 3.8 36.4 ± 3.8$^{*)}$	40.5 ± 1.9	105.0 ± 2.2 97.0 ± 2.1$^{*)}$
+0.78	38.9 ± 1.4	37.0 ± 2.3	63.0 ± 3.2		49.7 ± 3.0		23.1 ± 1.7	172.0 ± 3.1 146.0 ± 2.9$^{*)}$
+0.52	25.5 ± 1.0	50.0 ± 2.5 44.0 ± 2.4$^{*)}$	38.0 ± 2.2	118.0 ± 3.2 113.0 ± 3.1$^{*)}$	34.3 ± 2.5	49.5 ± 4.9 40.8 ± 4.9$^{*)}$		
+0.312	14.8 ± 0.8	70.0 ± 2.8 59.0 ± 2.7$^{*)}$	19.9 ± 1.5	140.0 ± 4.1 115.0 ± 4.0$^{*)}$	19.0 ± 2.0	70.2 ± 5.8 20.7 ± 5.8$^{*)}$		
Deuteron 1.04 GeV/c: mean = (20.4 ± 1.5) mip; r.m.s. = (95 ± 5)%								

*) Pedestals r.m.s. (U noise) subtracted.

Table 7

Mean ranges in number of absorber plates for different particles in the calorimeter structure No. 3. The dE/dx calculations are given in parentheses.

Beam momentum (GeV/c)	Muons	Protons	Deuterons
0.312	16.5 ± 1.0 (15.2 ± 0.5)		
0.52	32.0 ± 1.0 (31.5 ± 0.5)	2.0 ± 1.0 (2.4 ± 0.5)	
0.78	51.5 ± 1.0 (51.3 ± 0.5)	9.0 ± 1.0 (8.3 ± 0.5)	1.5 ± 1.0 (1.9 ± 0.5)
1.04	71.5 ± 1.5 (70.5 ± 0.5)	20.0 ± 1.0 (18.2 ± 0.5)	4.5 ± 1.0 (4.8 ± 0.5)
1.14	77.5 ± 2.0 (78.1 ± 0.5)		

Table 8

The mean calorimeter response in mip/GeV (A)
and the relative resolutions (r.m.s.) in per cent at 1.04 GeV/c
(B: data; C: calculations with the EGS4 Monte Carlo),
for different magnetic fields; 'slow' electronics;
data from the 1–6 GeV energy scan.

	Magnetic field (T)	0.0	0.5	0.7
Odd	A	30.9 ± 0.8	31.1 ± 0.5	32.0 ± 0.5
	B	53.7 ± 2.0	60.1 ± 2.0	64.4 ± 1.5
	C	50.0 ± 5.0	62.7 ± 4.0	68.8 ± 5.0
Even	A	31.4 ± 0.8	31.1 ± 0.6	32.1 ± 0.8
	B	51.4 ± 1.5	51.3 ± 2.2	51.7 ± 1.8
	C	49.0 ± 5.0	52.3 ± 3.0	54.9 ± 4.0
Total	A	62.4 ± 1.1	62.2 ± 0.8	64.1 ± 1.0
	B	36.3 ± 1.5	38.9 ± 1.0	42.7 ± 1.5
	C	35.0 ± 3.0	39.8 ± 2.0	44.0 ± 3.0

Table 9

The r.m.s. and standard deviation (both in mip) of a Gaussian fit
to U noise (pedestal) distribution for the sum of 56 chambers.
Ar (80%) + CO_2 (20%) mixture.

Electronics	Calorimeter structure			
	No. 1: No shield		No. 3: 1 mm Cu shield	
	r.m.s.	st. dev.	r.m.s.	st. dev.
Fast	14.5 ± 2.0	11.3 ± 1.6	7.0 ± 1.0	5.4 ± 0.8
Slow	28.5 ± 1.4	26.6 ± 1.3	13.1 ± 0.7	10.1 ± 0.5

Figure captions

Fig. 1: The experimental set-up at the ITEP.

Fig. 2: Time-of-flight spectrum of positive beam particles at 2.08 GeV/c.

Fig. 3: The normalized amplitude spectra of the single-chamber plane for 6 GeV/c pions. Structure No. 3.

Fig. 4: Parameters of the reconstructed spike spectrum (see text) versus beam energy for pions. The size of the points corresponds to the statistical reconstruction error: a) the mean amplitude of spikes A_{spike} in mip; b) the mean number of spikes per event N_{spike}.

Fig. 5: Transverse (a) and longitudinal (b) distributions of 'spikes' at 6 GeV/c due to neutron interactions with hydrogen nuclei in the gas (histograms). Structure No. 3. Dashed lines represent the smoothed ordinary hadron-shower component [6 GeV/c; Ar (80%) + CO_2 (20%)].

Fig. 6: Total calorimeter response to 2 GeV/c pions. The histogram is the experimental distribution; the solid line is the result of the convolution of the experimental Ar + CO_2 distribution and the spectrum of spikes due to the neutron interactions with hydrogen in isobutane (see text). Structure No. 3.

Fig. 7: The electron (circles), pion (squares) and muon (triangles) response of the calorimeter for two Ar + CO_2 mixtures: (10 + 90)% (full data points) and (80 + 20)% (open data points). Fast-electronics gates are 300 ns for the (80 + 20)% mixture and 400 ns for the (10 + 90)% mixture. The straight lines are the linear fit in the range 2–6 GeV/c.

Fig. 8: The π/e ratio of the calorimeter responses (at equal kinetic energy) versus the 'linear density' of the absorber for two gas fillings at 2.08 GeV/c. Slow electronics, no shield. Full data points: the 'full calorimeter method' (data from ref. [5] and table 4), open data points: the results of the 'single-chamber scan' (table 3); squares: isobutane; circles: the Ar + CO_2 mixture. The solid line is the Monte Carlo calculation for the difference between the isobutane and Ar + CO_2 responses. The dashed line for the Ar + CO_2 points is drawn to guide the eye.

Fig. 9: The pion (squares) and the electron (circles) response for a chamber filled with isobutane for two U-absorber shielding structures: 1 mm Cu (open points, structure No. 3); 2 mm Plexiglas (full points, structure No. 2). The straight lines are to guide the eye.

Fig. 10: The mean electron response as a function of ΔE_{mip}, the energy loss of a minimum-ionizing particle in one absorber layer. The points correspond to different absorber structures (from left to right): 4.5 mm U, no shield; 4.5 mm U, 2 mm Plexiglas shield; 4.5 mm U, 1 mm Cu shield; 9.0 mm U, no shield. Slow electronics. The line is the $1/\Delta E_{\mathrm{mip}}$ dependence.

Fig. 11: Pion response for different U absorber shielding structures and two gas mixtures, Ar (80%) + CO_2 (20%) (full points) and isobutane (open points), as a function of ΔE_{mip}, the energy loss of a minimum-ionizing particle in one absorber layer. The pion response is in mip/GeV

of pion kinetic energy. The beam momentum is 2 GeV/c. The period of calorimeter structure is 18 mm. The points correspond to different absorber structures (from left to right): 4.5 mm U, no shield; 4.5 mm U, 2 mm Plexiglas shield; 4.5 mm U, 1 mm Cu shield. Slow electronics. The line is the $1/\Delta E_{mip}$ dependence. The 'diamonds' are Monte Carlo calculations (see text).

Fig. 12: The muon-pion separation at 0.5 GeV/c. The log W is the value of the likelihood function.

Fig. 13: The calorimeter responses (in mip) for different incident particles for: a) Ar (80%) + CO_2 (20%); b) isobutane. For muons with kinetic energies > 1.1 GeV the responses are plotted versus the calculated energy deposit in the calorimeter. Calorimeter structure No. 3.

Fig. 14: The averaged longitudinal shower profiles for protons a) 2.08 GeV/c and b) 1.04 GeV/c for the Ar (80%) + CO_2 (20%) mixture. The calculated range for 1.04 GeV/c protons is indicated by an arrow. Structure No. 3.

Fig. 15: The electron/hadron and electron/muon response ratios extrapolated to equal kinetic energy for the Ar (80%) + CO_2 (20%) mixture. Structure No. 3; slow electronics. The dashed line shows the averaged value for the electron/muon ratio.

Fig. 16: The electron/hadron and electron/muon response ratios extrapolated to equal kinetic energy for isobutane: a) negative beam ; b) positive beam. Structure No. 3; slow electronics. The dashed lines show the averaged values for the electron/muon ratio.

Fig. 17: The energy resolution for the electrons (open circles, 20 chamber planes taken) and for the stopped muons (filled circles, 86 chamber planes integrated). Structure No. 3; Ar (80%) + CO_2 (20%); slow electronics. The horizontal scale is proportional to $1/\sqrt{E_{kin}(GeV)}$. a) The Gaussian fit; U noise not subtracted. b) The r.m.s. values; U noise subtracted.

Fig. 18: The 6 GeV/c pion response (86 chamber planes integrated). The r.m.s. of the distribution is (33 ± 2)%; the standard deviation of a fitted Gaussian (continuous line) is (29 ± 2)%. Structure No. 3; Ar (80%) + CO_2 (20%); slow electronics.

Fig. 19: Structure No. 3; Ar (80%) + CO_2 (20%); slow and fast electronics. a) Pion and proton responses (in mip) versus kinetic energy. The lines are to guide the eye. b) The standard deviation of the Gaussian fit to measured amplitude distributions for pions (open circles) and protons (full circles) versus E_{kin}. The vertical scale is in mip without subtraction of the U-noise contribution divided by $\sqrt{E_{kin}(GeV)}$. The Gaussian resolution for stopping muons (triangles) is shown for comparison. Horizontal lines are fits to data above 0.4 GeV.

Fig. 20: The mean values of the first three highest amplitudes (out of a total of 688) S1, S2, and S3 in an event as a function of incident pion momentum. Structure No. 3; isobutane; slow electronics.

Fig. 21: The calorimeter response to 4.6 GeV/c pions: a) for Ar (80%) + CO_2 (20%); b) for isobutane. Dashed lines are raw data, solid lines are the same data after the LSM (see text). Structure No. 3; slow electronics.

Fig. 22: The r.m.s. resolution before (open points) and after (full points) application of the LSM (see text), for two chamber gases: a) Ar (80%) + CO_2 (20%); b) isobutane. For Ar + CO_2, the Gaussian fit resolution is also shown (crosses). The horizontal scale is $1/\sqrt{E_{kin}(GeV)}$. Structure No. 3; slow electronics. U noise is not subtracted. The lines are to guide the eye.

Fig. 23: Double-chamber calorimeter response to 2 GeV/c pions. Dashed line: odd planes; solid line: 1/2(odd + even) planes. (Ar + CO_2) + (Ar + CO_2) (80 + 20) combination. Structure No. 5.

Fig. 24: Double-chamber calorimeter response to 2 GeV/c pions with the spike rejection procedure applied (see text). The histogram is for 1/2(odd + even) planes. The solid curve is the Gaussian fit to the histogram. (Ar + CO_2) + (Ar + CO_2) (80 + 20) combination. Structure No. 5.

Fig. 25: Double-chamber calorimeter structure. The r.m.s. resolution for pions (in mip) divided by $\sqrt{E_{kin}(GeV)}$ versus pion beam energy: a) for the gas combination (Ar + CO_2) + (Ar + CO_2) (80 + 20); b) for the gas combination isobutane + isobutane. Triangles correspond to odd (or even) chambers; squares to the odd + even; circles to the odd + even with the spike rejection procedure applied.

Fig. 26: Double-chamber calorimeter response for two gas combinations. Pions are shown for the gas combinations isobutane + isobutane (circles) and for (Ar + CO_2) + (Ar + CO_2) (squares). The electrons are also shown (triangles). Open points (1) before and full points (2) after the application of the spike rejection cut (see text). The lines are to guide the eye.

Fig. 27: The relative electron resolution (r.m.s.) at 1 GeV for the electromagnetic section of the calorimeter operating in the magnetic field. The circles are for the response of odd chamber planes (with proportional tubes parallel to the field); triangles are for even planes (wires perpendicular to the field). The squares are the resolution for total 17 planes. The lines are to guide the eye.

Fig. 28: The muon response in keV for a chamber in front of uranium (open points) and behind 4.5 cm (10 plates) of uranium (full points). In the latter position the chamber is shielded by 1 mm Cu sheets. Gas mixture Ar (80%) + CO_2 (20%).

Fig. 29: The gate-width scan. Full points are the r.m.s. of U noise, expressed in GeV, of the electron response equivalent (79 chambers). Open points are 1 GeV electron resolution in per cent (20 chambers). The pion/electron ratio measured at 4 GeV is shown by triangles. Structure No. 4; Ar (80%) + CO_2 (20%); fast electronics.

Fig. 30: The pedestal distribution at 300 ns gate width for 79 chambers. Structure No. 4; Ar (80%) + CO_2 (20%); fast electronics; 1 mip = 17.5 LRS 2249A ADC channels. The r.m.s. of the distribution is 8.9 mip; the standard deviation of the Gaussian fit is 6.5 mip.

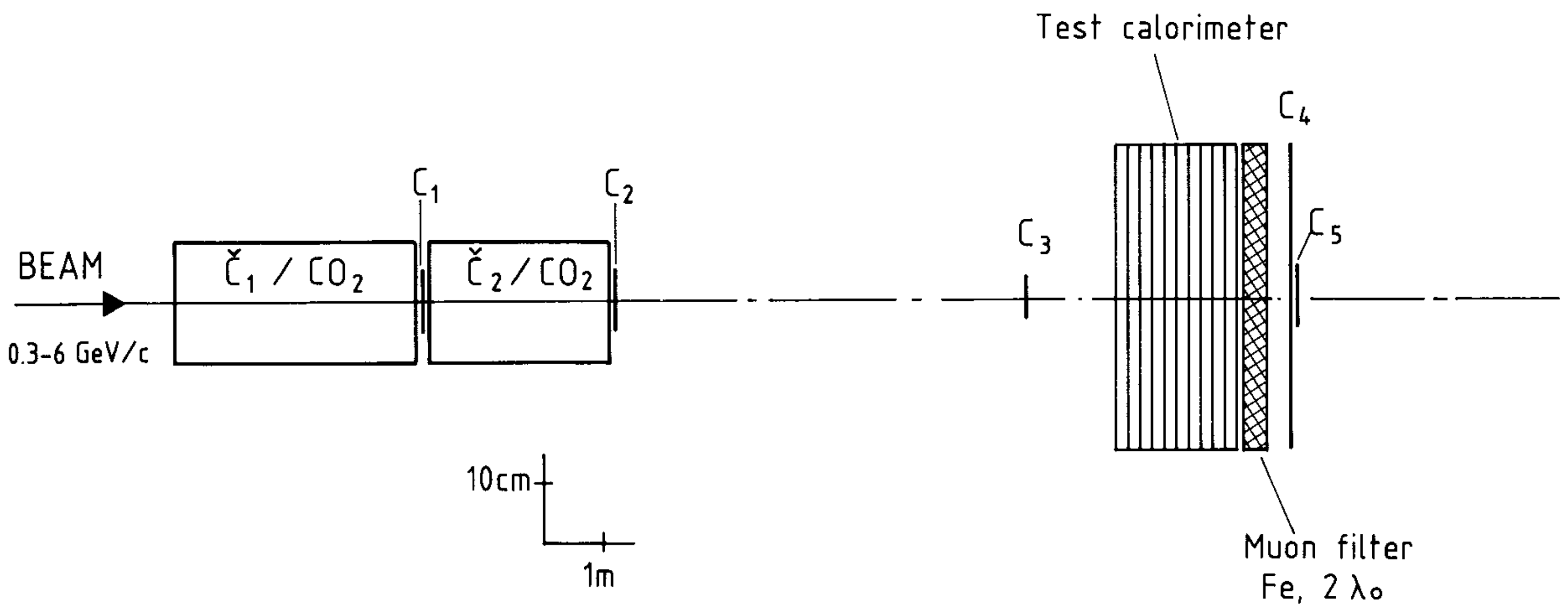
Test calorimeter
C$_4$
C$_1$
C$_2$
C$_3$
C$_5$
BEAM
Č$_1$ / CO$_2$
Č$_2$ / CO$_2$
0.3-6 GeV/c
10cm
1m
Muon filter
Fe, 2 λo

Fig. 1

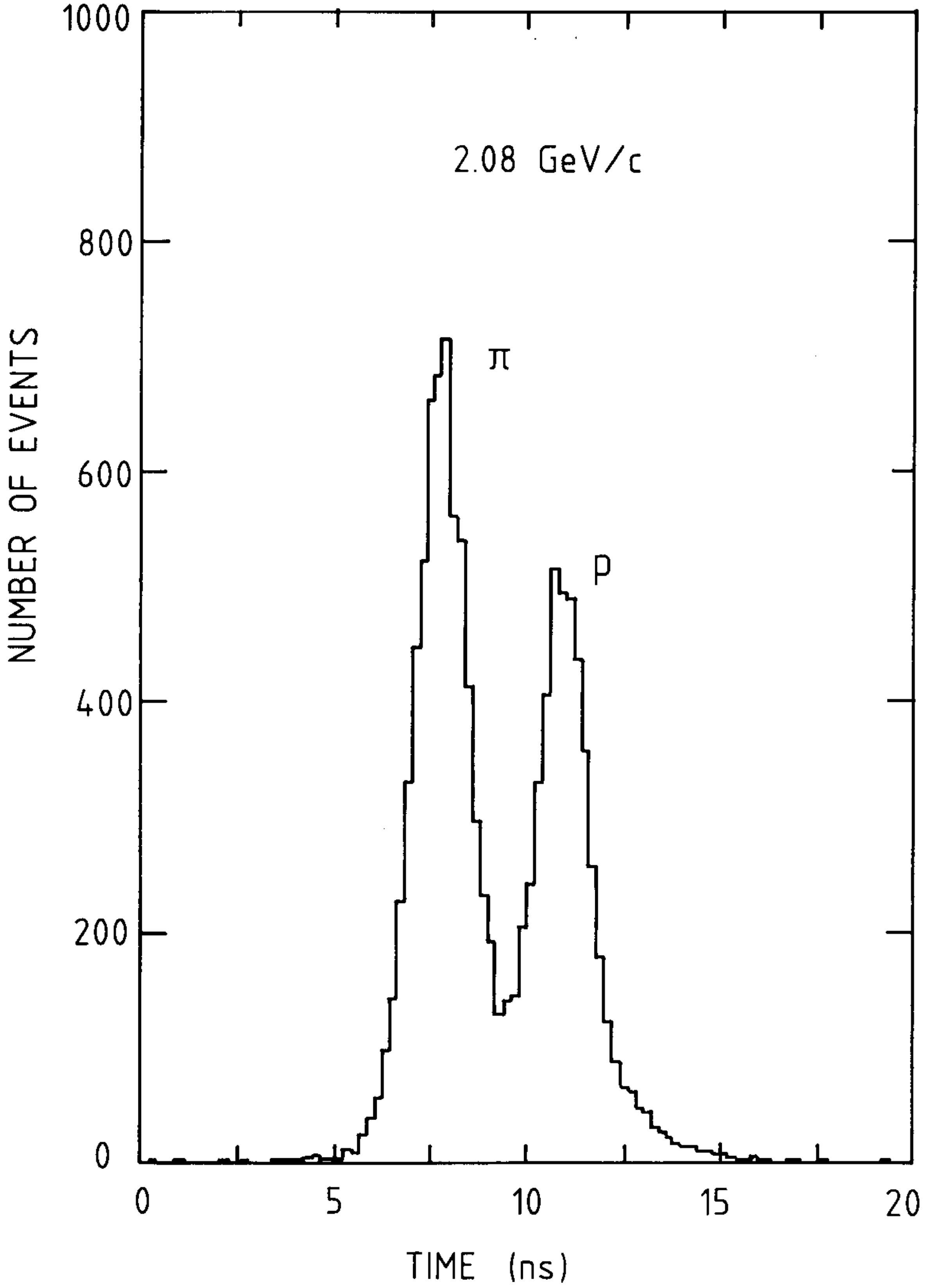
2.08 GeV/c
π
p
NUMBER OF EVENTS
TIME (ns)
0
200
400
600
800
1000
0
5
10
15
20

Fig. 2

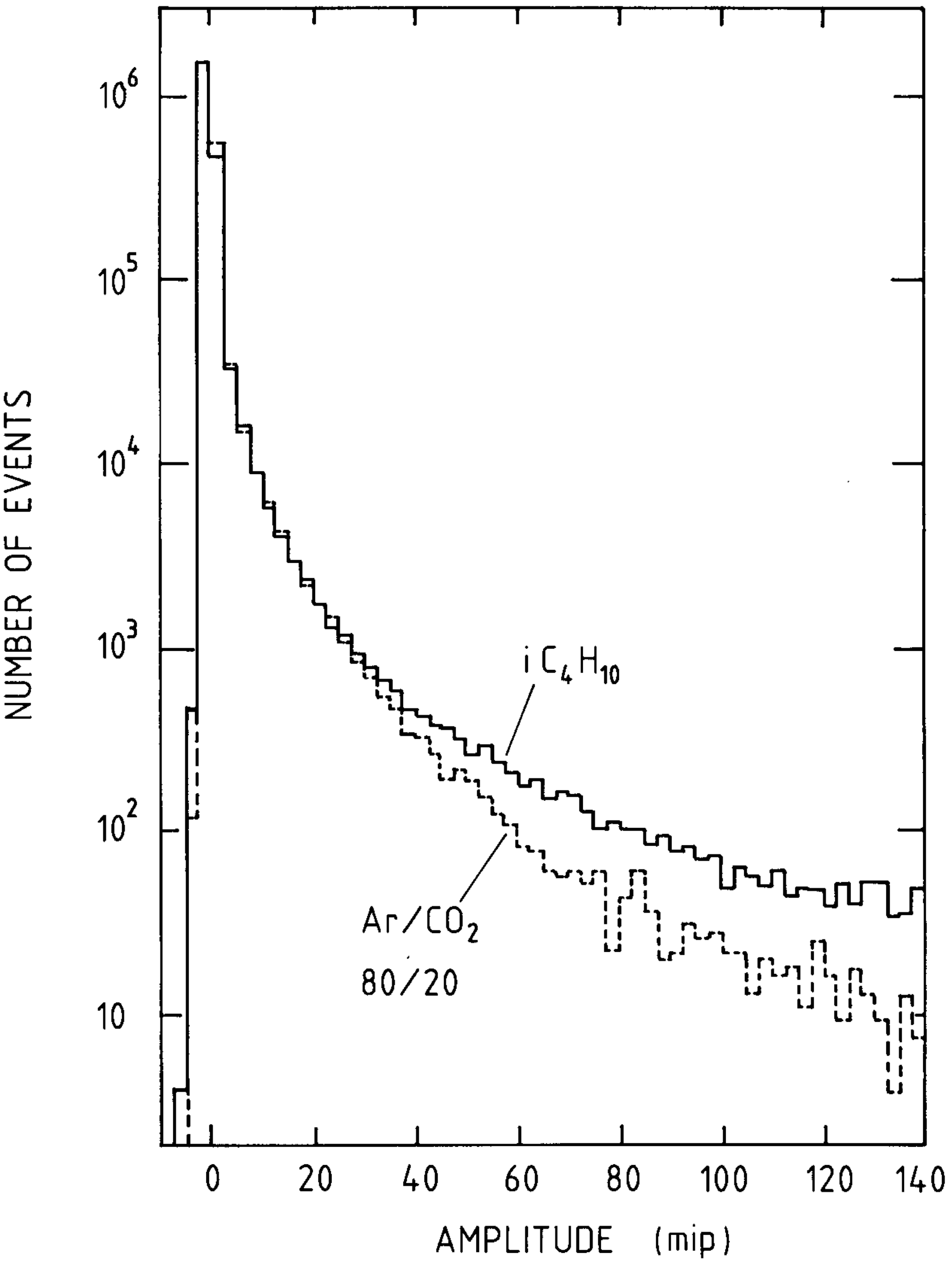
NUMBER OF EVENTS
10^6
10^5
10^4
10^3
10^2
10
iC_4H_{10}
Ar/CO_2
80/20
0
20
40
60
80
100
120
140
AMPLITUDE (mip)

Fig. 3

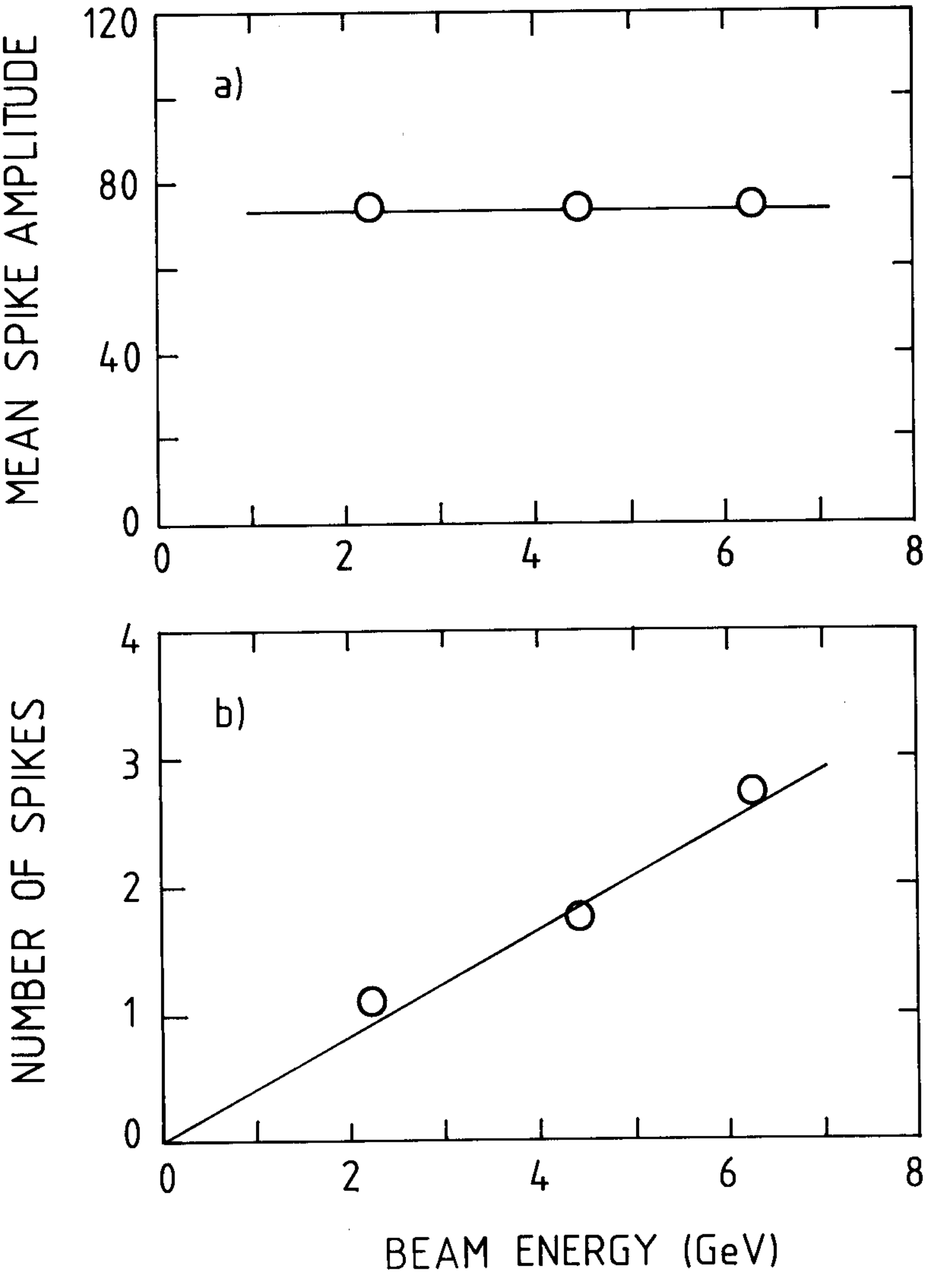
a)
MEAN SPIKE AMPLITUDE
0
40
80
120
0
2
4
6
8
b)
NUMBER OF SPIKES
0
1
2
3
4
0
2
4
6
8
BEAM ENERGY (GeV)

Fig. 4

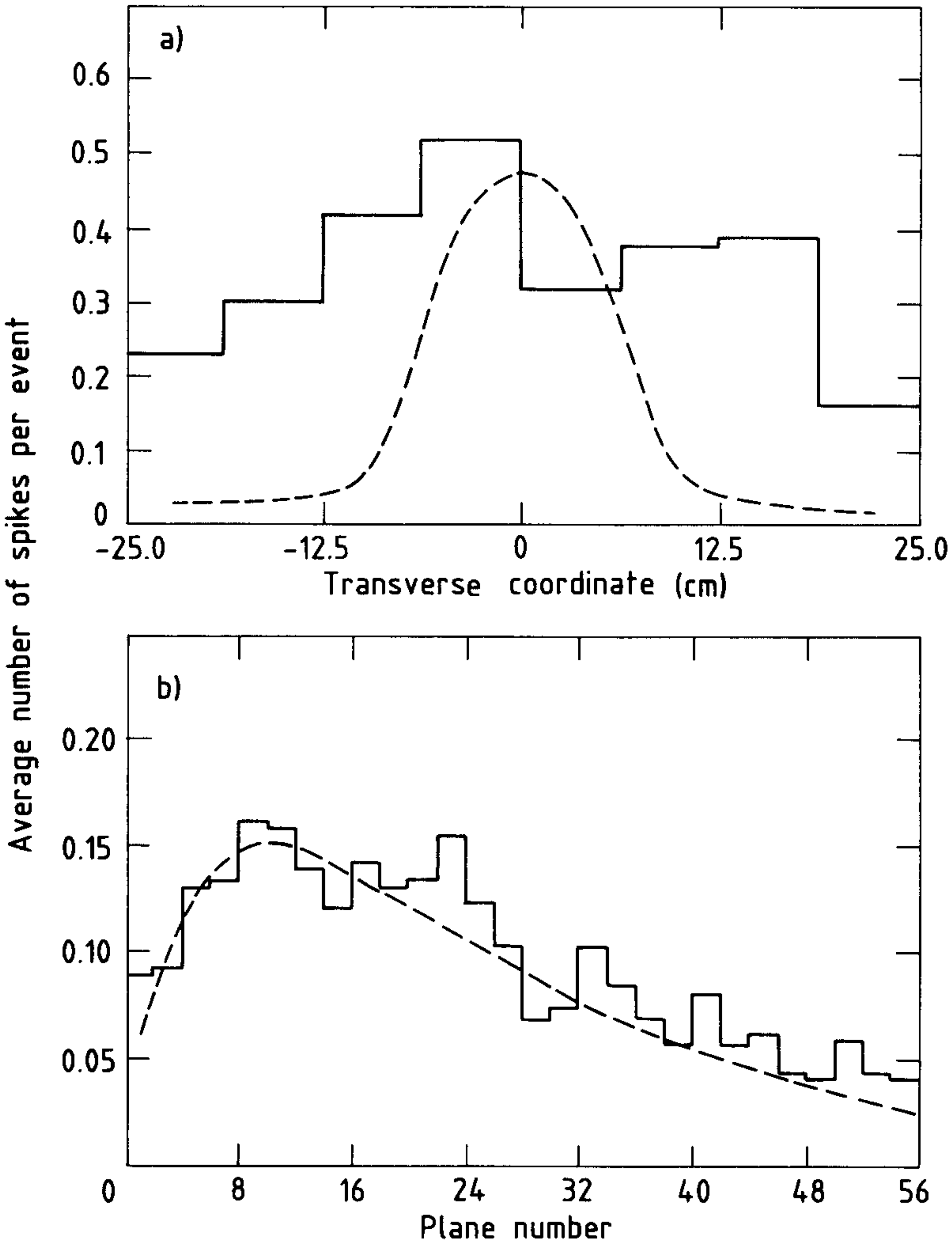
a)
0.6
0.5
0.4
0.3
0.2
0.1
0
-25.0
-12.5
0
12.5
25.0
Transverse coordinate (cm)
Average number of spikes per event
b)
0.20
0.15
0.10
0.05
0
8
16
24
32
40
48
56
Plane number

Fig. 5

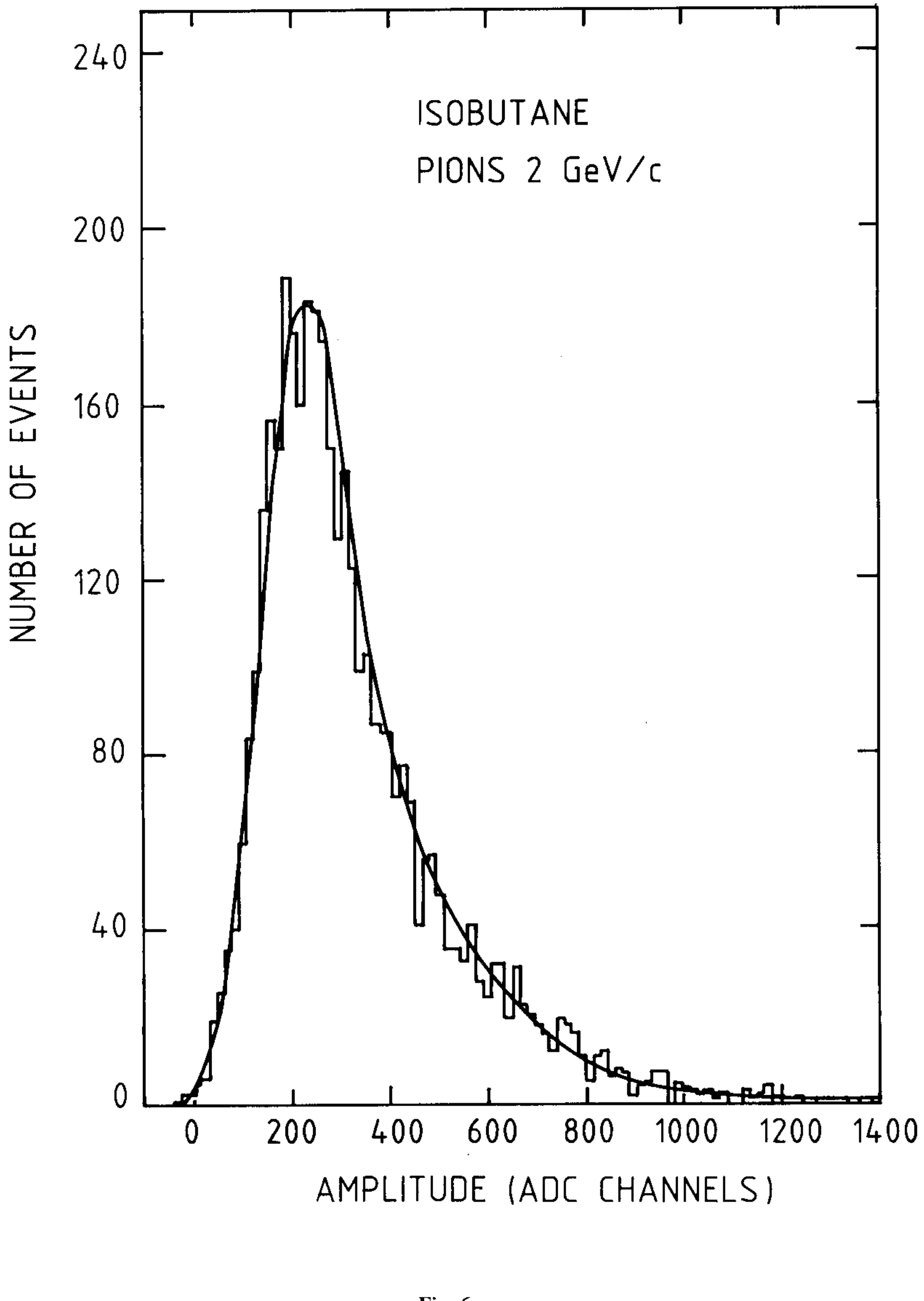
ISOBUTANE
PIONS 2 GeV/c
NUMBER OF EVENTS
240
200
160
120
80
40
0
0
200
400
600
800
1000
1200
1400
AMPLITUDE (ADC CHANNELS)

Fig. 6

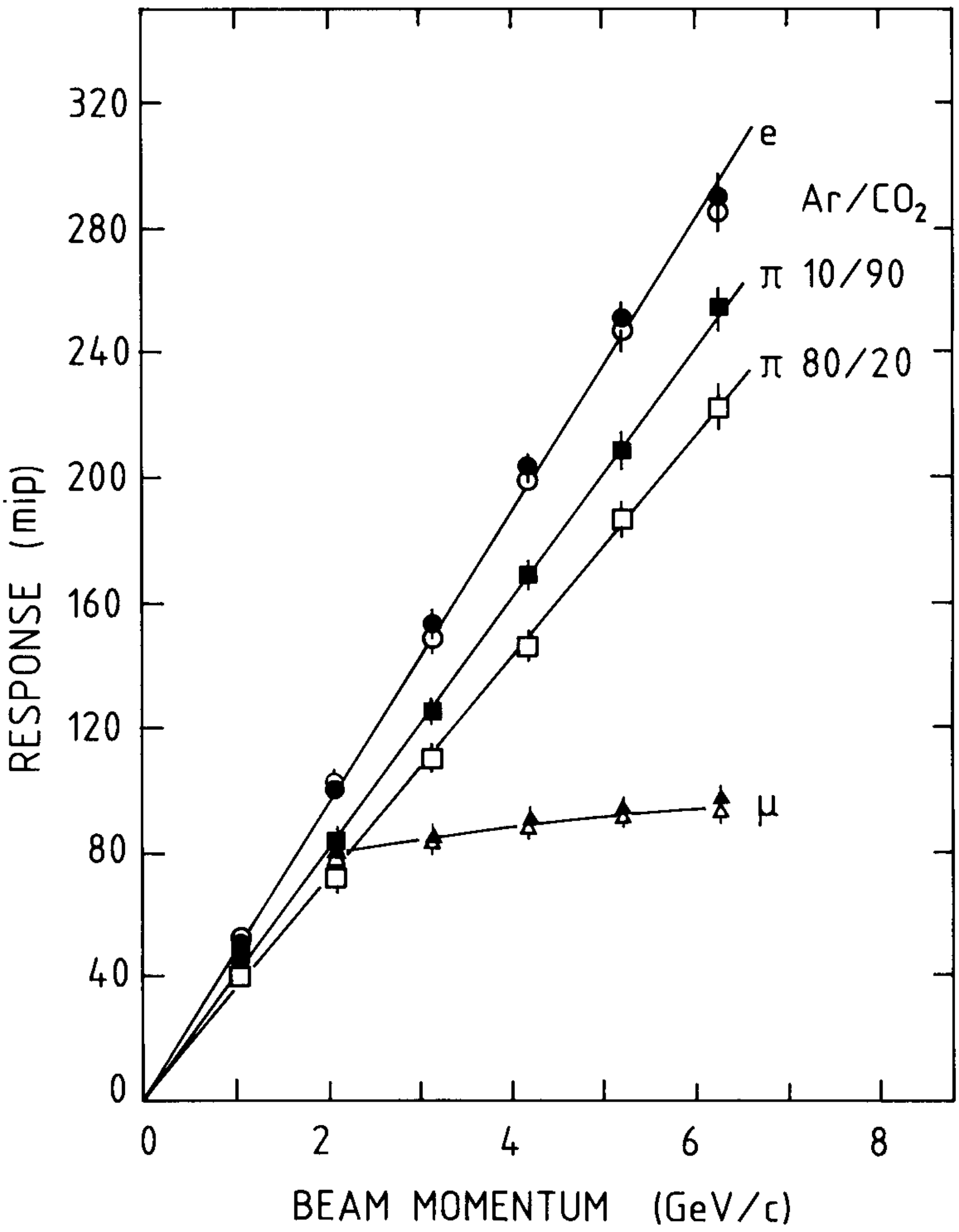
RESPONSE (mip)
BEAM MOMENTUM (GeV/c)
0
40
80
120
160
200
240
280
320
0
2
4
6
8
e
Ar/CO₂
π 10/90
π 80/20
μ

Fig. 7

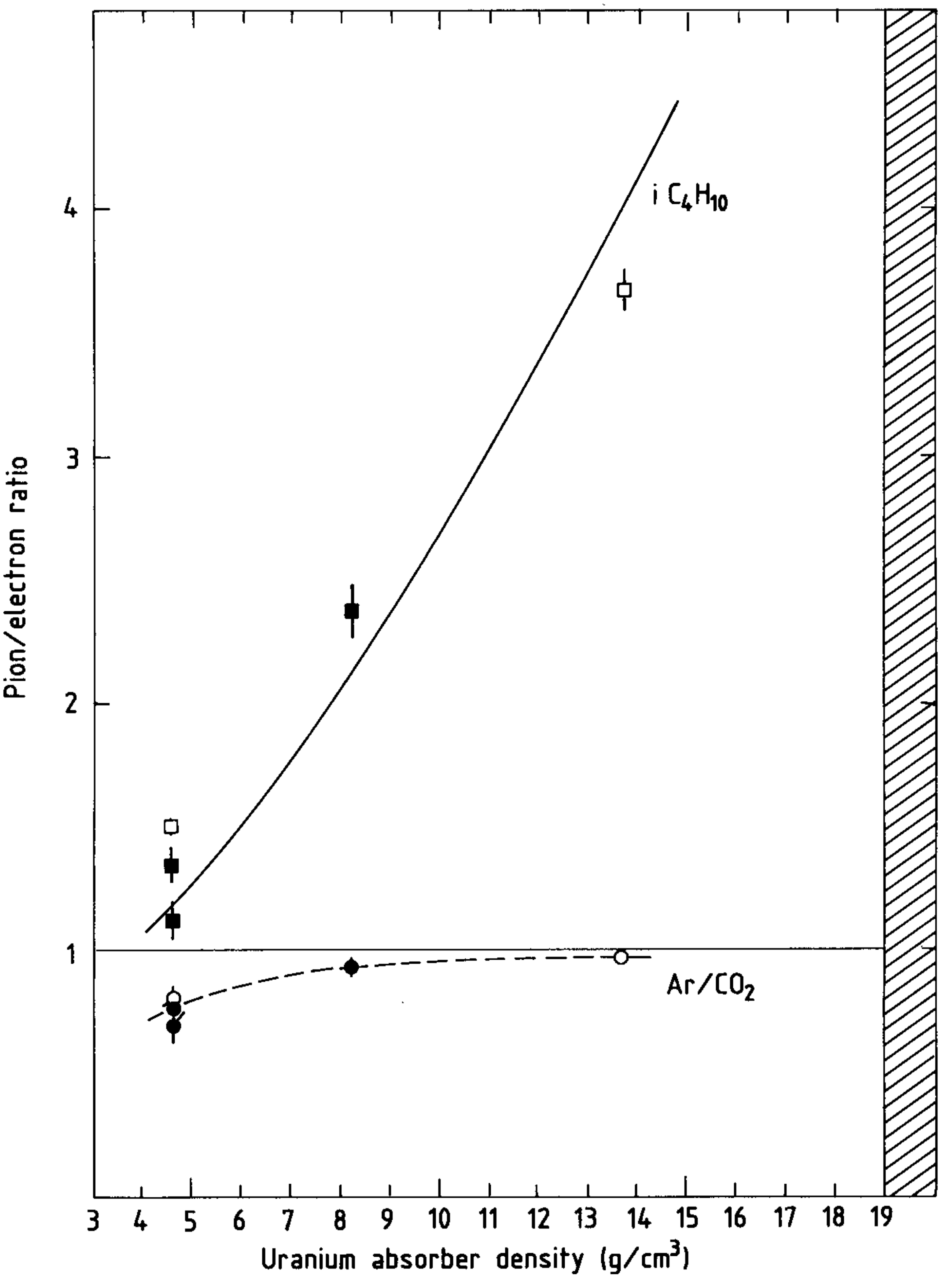
Pion/electron ratio
4
3
2
1
iC_4H_{10}
Ar/CO_2
3
4
5
6
7
8
9
10
11
12
13
14
15
16
17
18
19
Uranium absorber density (g/cm^3)

Fig. 8

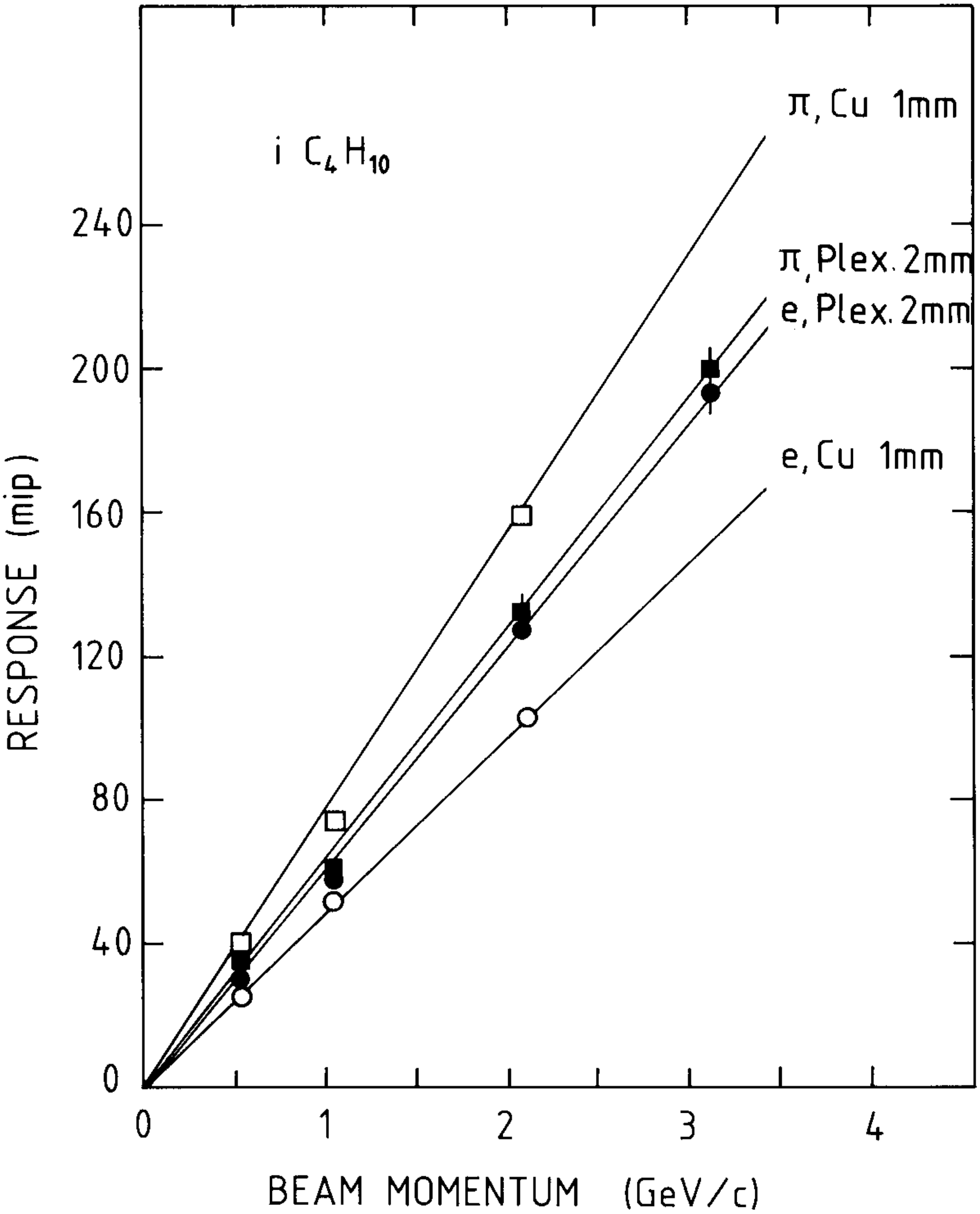
i C_4H_{10}
π, Cu 1mm
π, Plex. 2mm
e, Plex. 2mm
e, Cu 1mm
RESPONSE (mip)
0
40
80
120
160
200
240
BEAM MOMENTUM (GeV/c)
0
1
2
3
4

Fig. 9

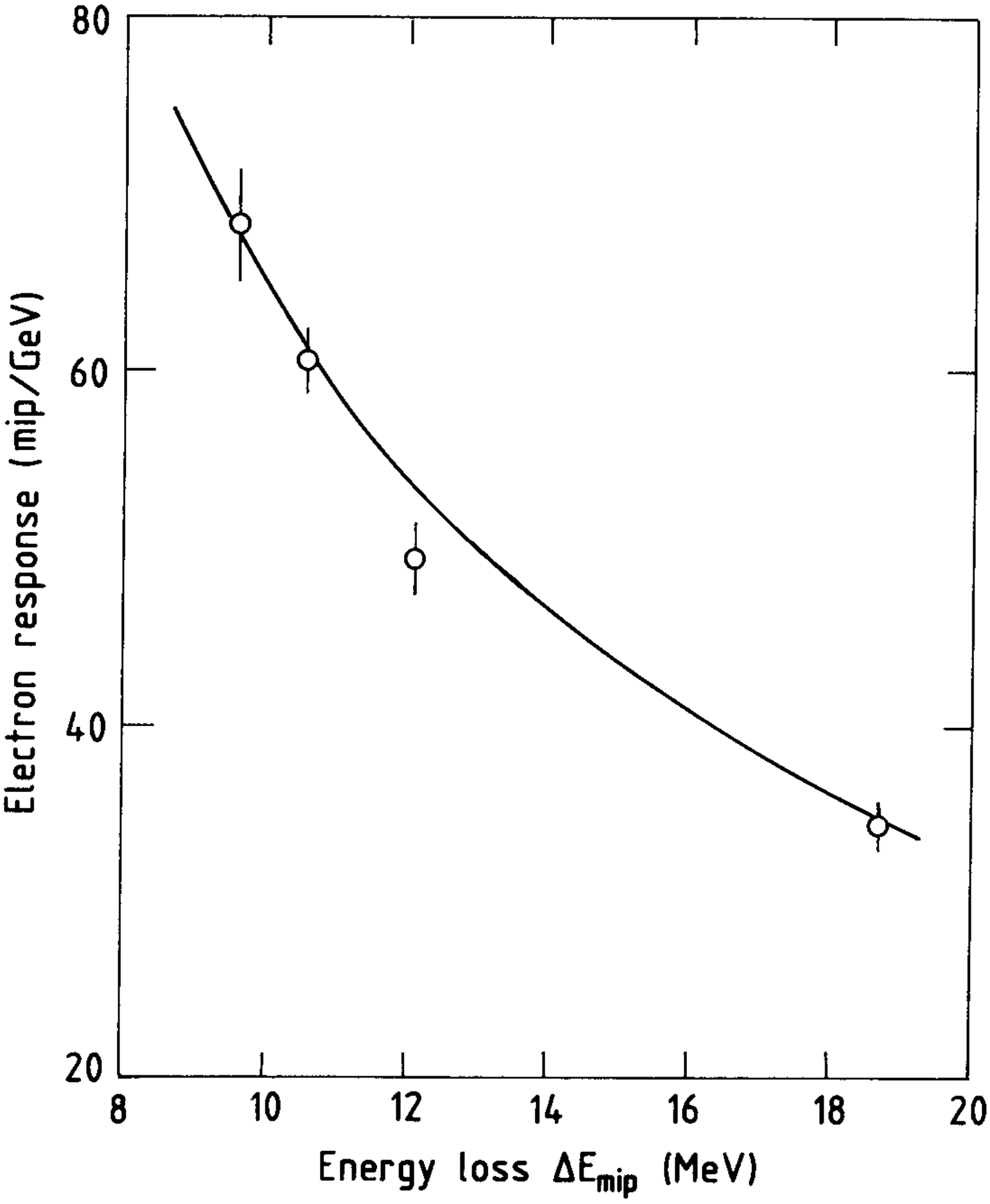
80
60
40
20
Electron response (mip/GeV)
8
10
12
14
16
18
20
Energy loss ΔE_{mip} (MeV)

Fig. 10

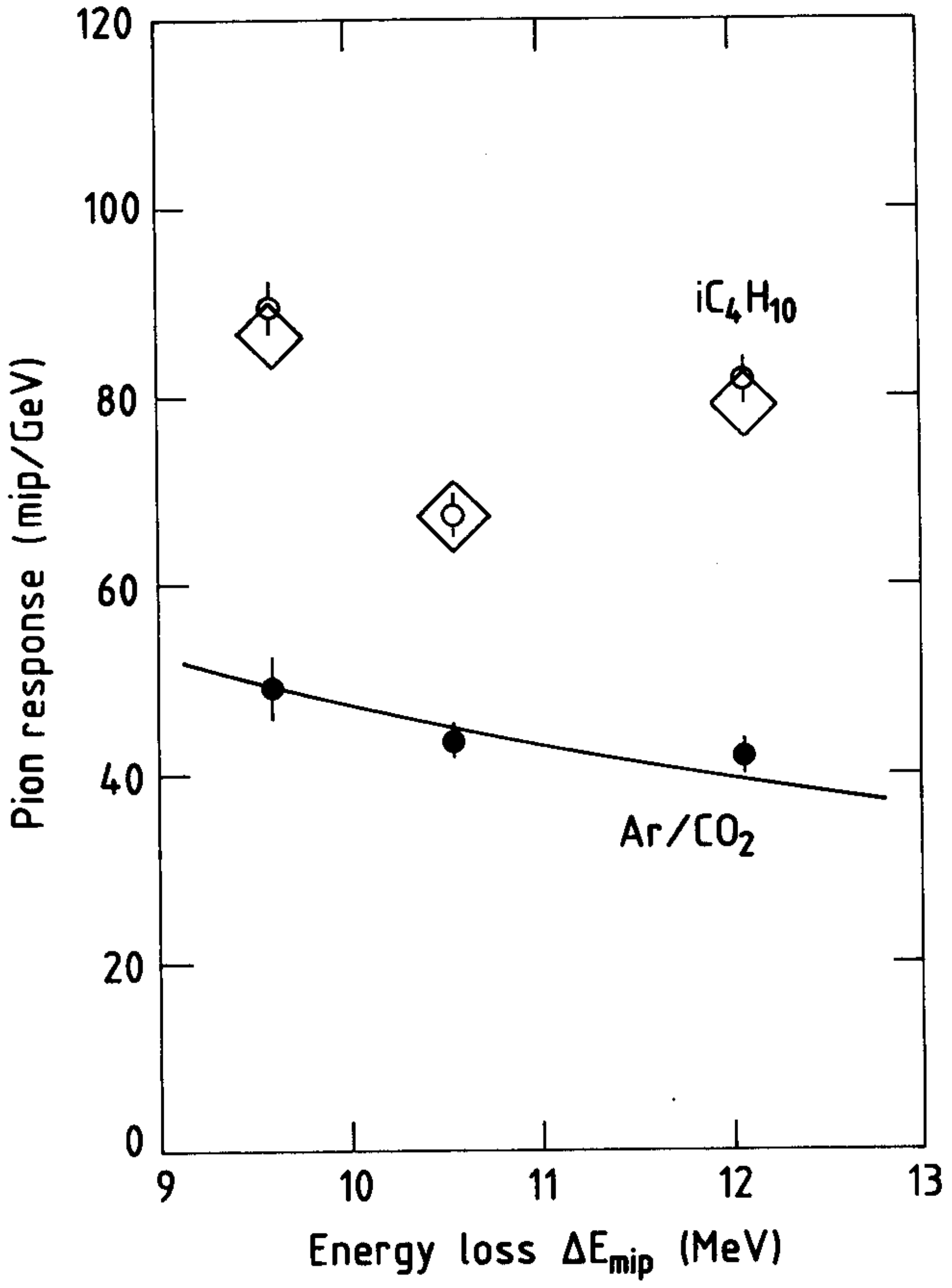

120
100
80
60
40
20
0
Pion response (mip/GeV)
9
10
11
12
13
Energy loss ΔE_{mip} (MeV)
iC_4H_{10}
Ar/CO_2

Fig. 11

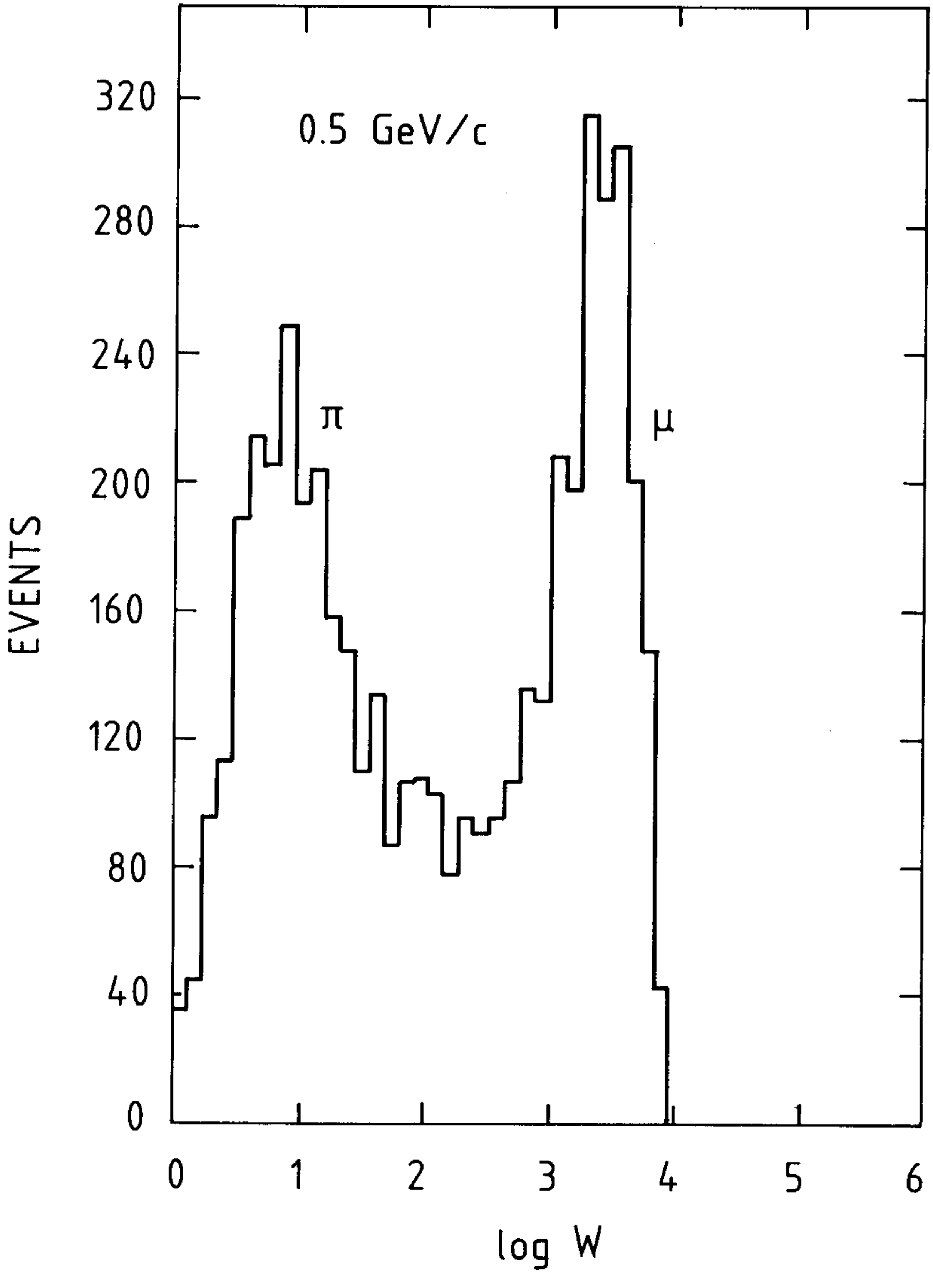

Fig. 12

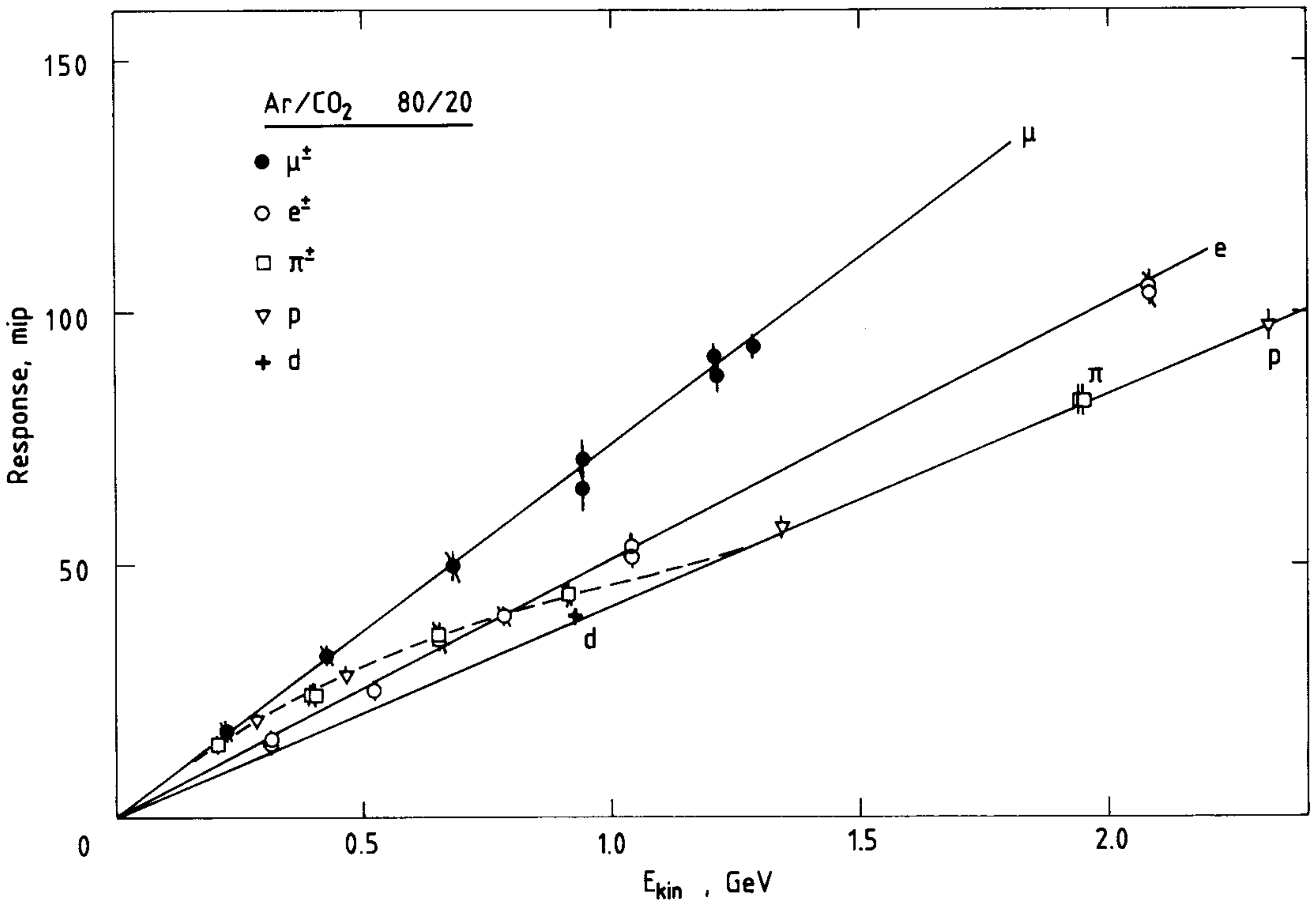
Ar/CO_2 80/20
● $\mu^{\pm}$
○ $e^{\pm}$
□ $\pi^{\pm}$
▽ p
✚ d
μ
e
π
p
d
Response, mip
150
100
50
0
0.5
1.0
1.5
2.0
E_{kin} , GeV

Fig. 13 a

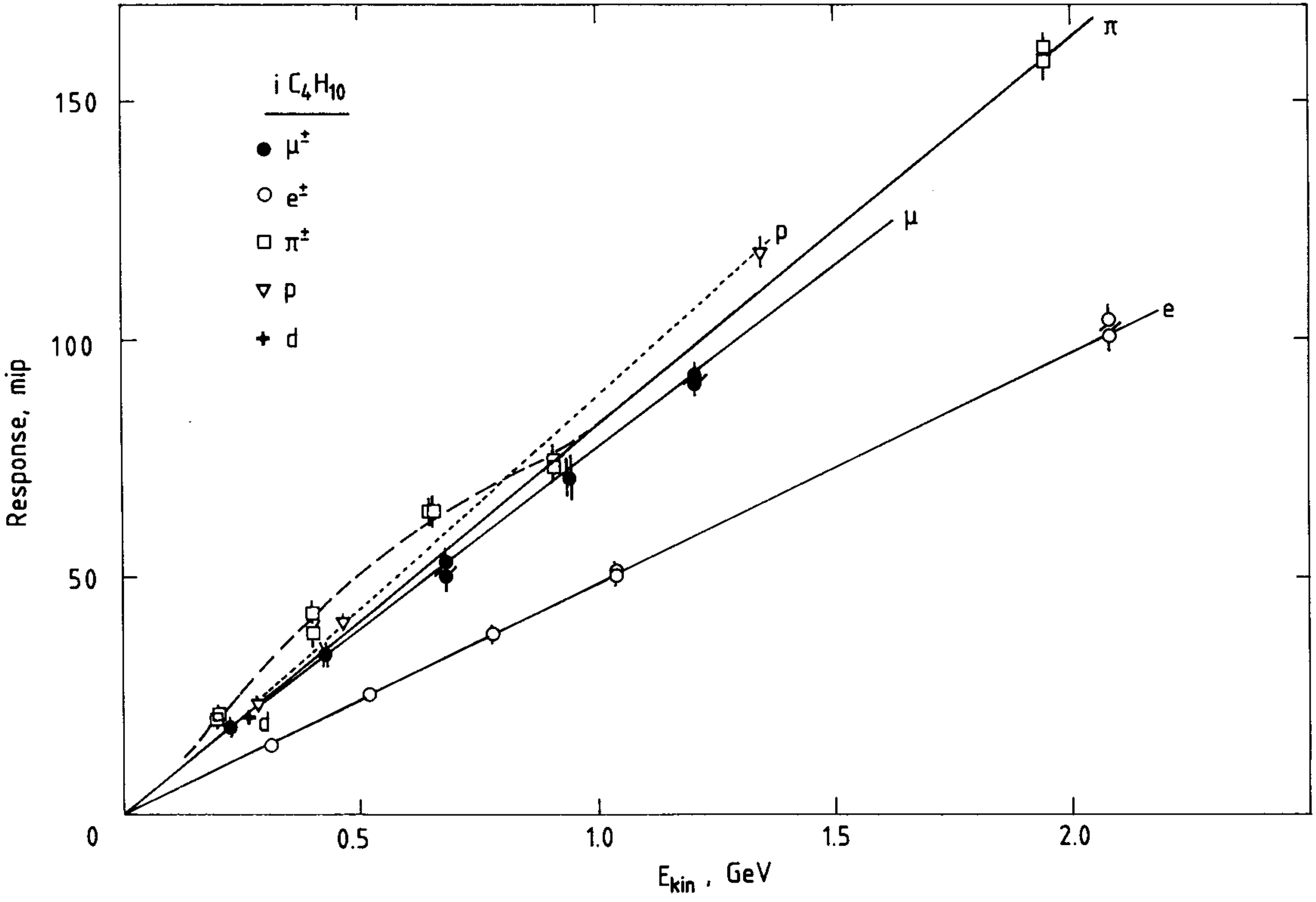
i C4H10
μ±
e±
π±
p
d
Response, mip
150
100
50
0
0.5
1.0
1.5
2.0
Ekin , GeV
π
μ
p
e
d

Fig. 13 b

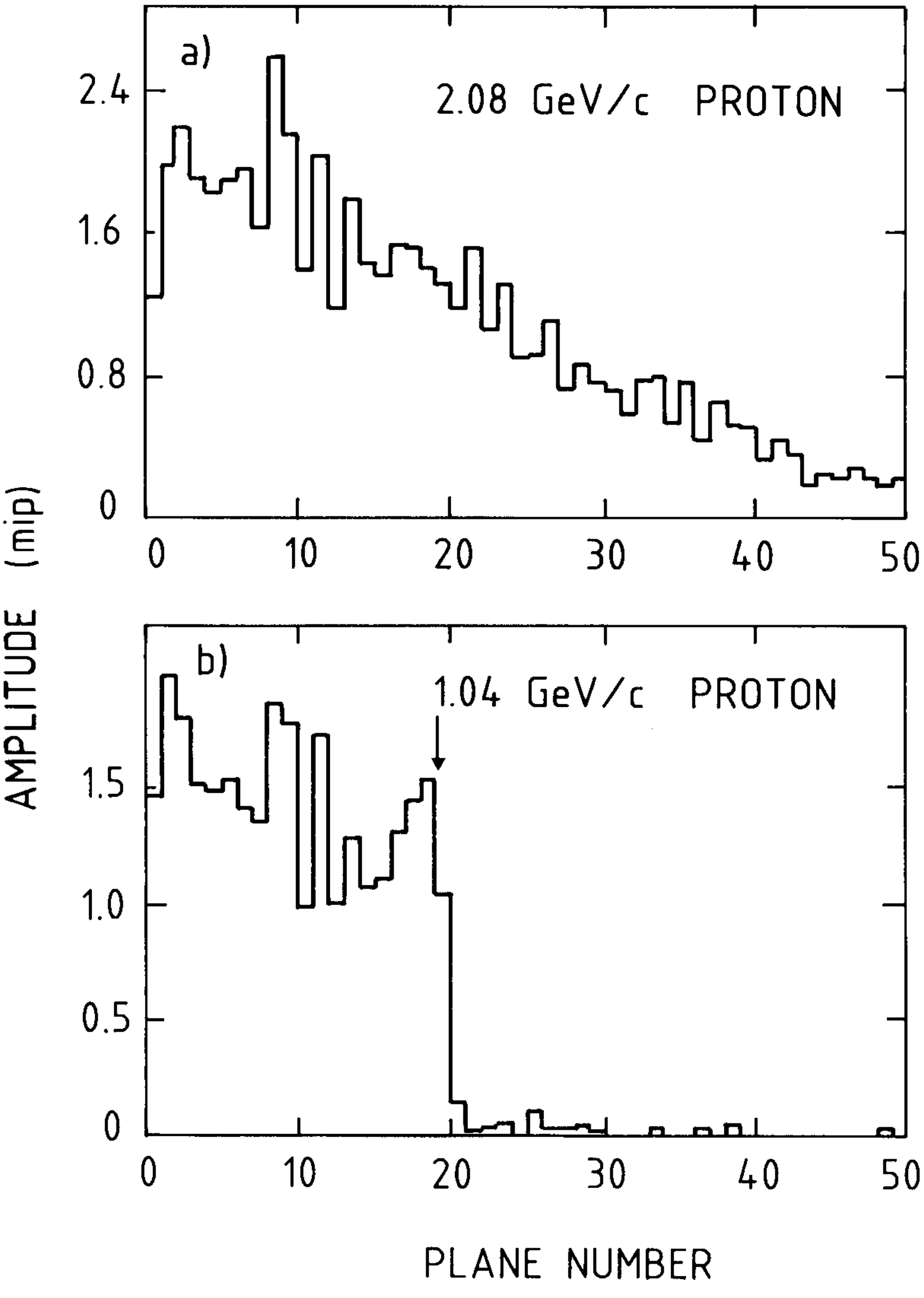

a)
2.08 GeV/c PROTON
2.4
1.6
0.8
0
0
10
20
30
40
50
AMPLITUDE (mip)
b)
1.04 GeV/c PROTON
1.5
1.0
0.5
0
0
10
20
30
40
50
PLANE NUMBER

Fig. 14

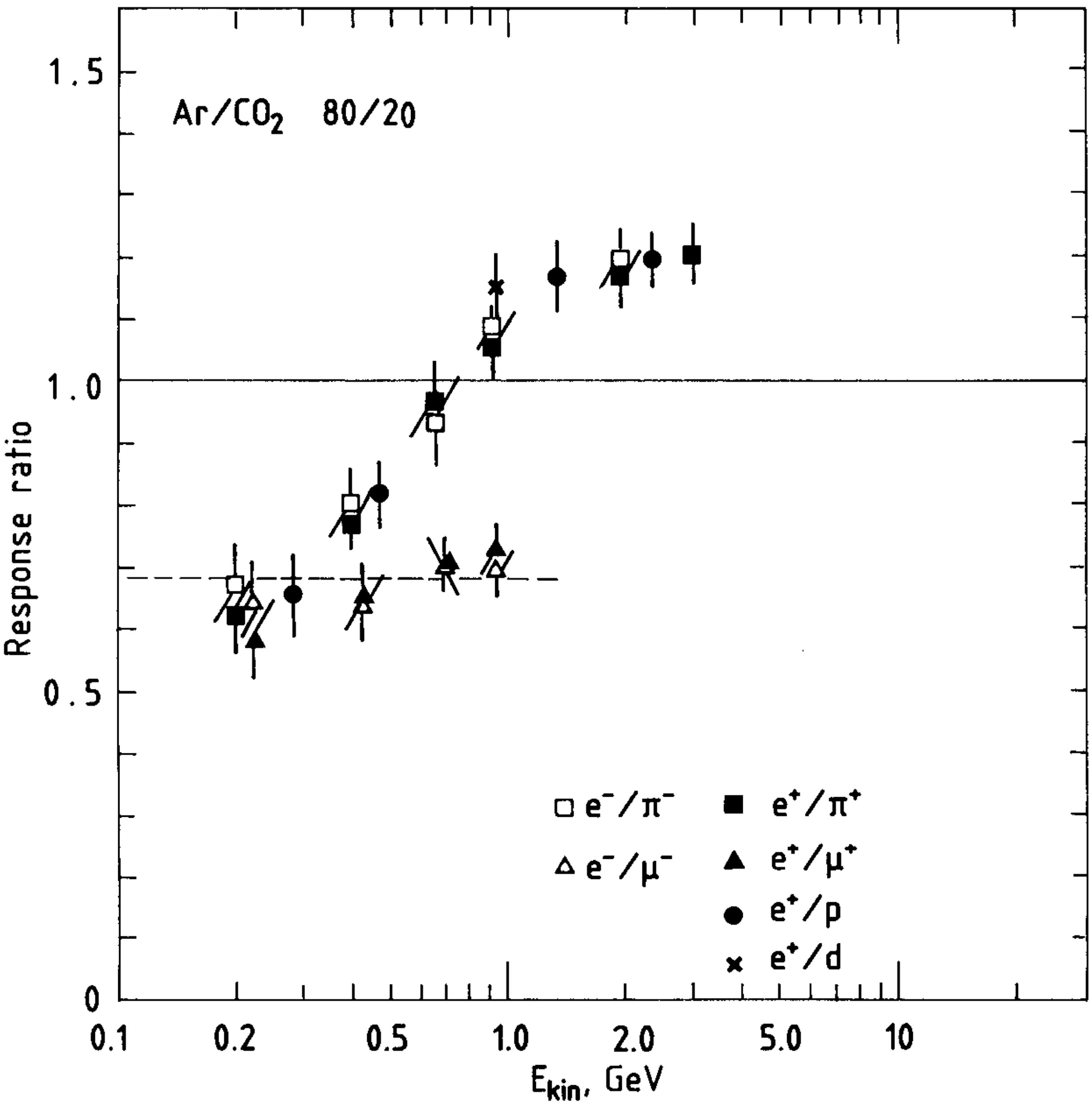
Ar/CO$_2$ 80/20
Response ratio
1.5
1.0
0.5
0
0.1
0.2
0.5
1.0
2.0
5.0
10
E$_{kin}$, GeV
□ e$^-$/π$^-$
■ e$^+$/π$^+$
△ e$^-$/μ$^-$
▲ e$^+$/μ$^+$
● e$^+$/p
× e$^+$/d

Fig. 15

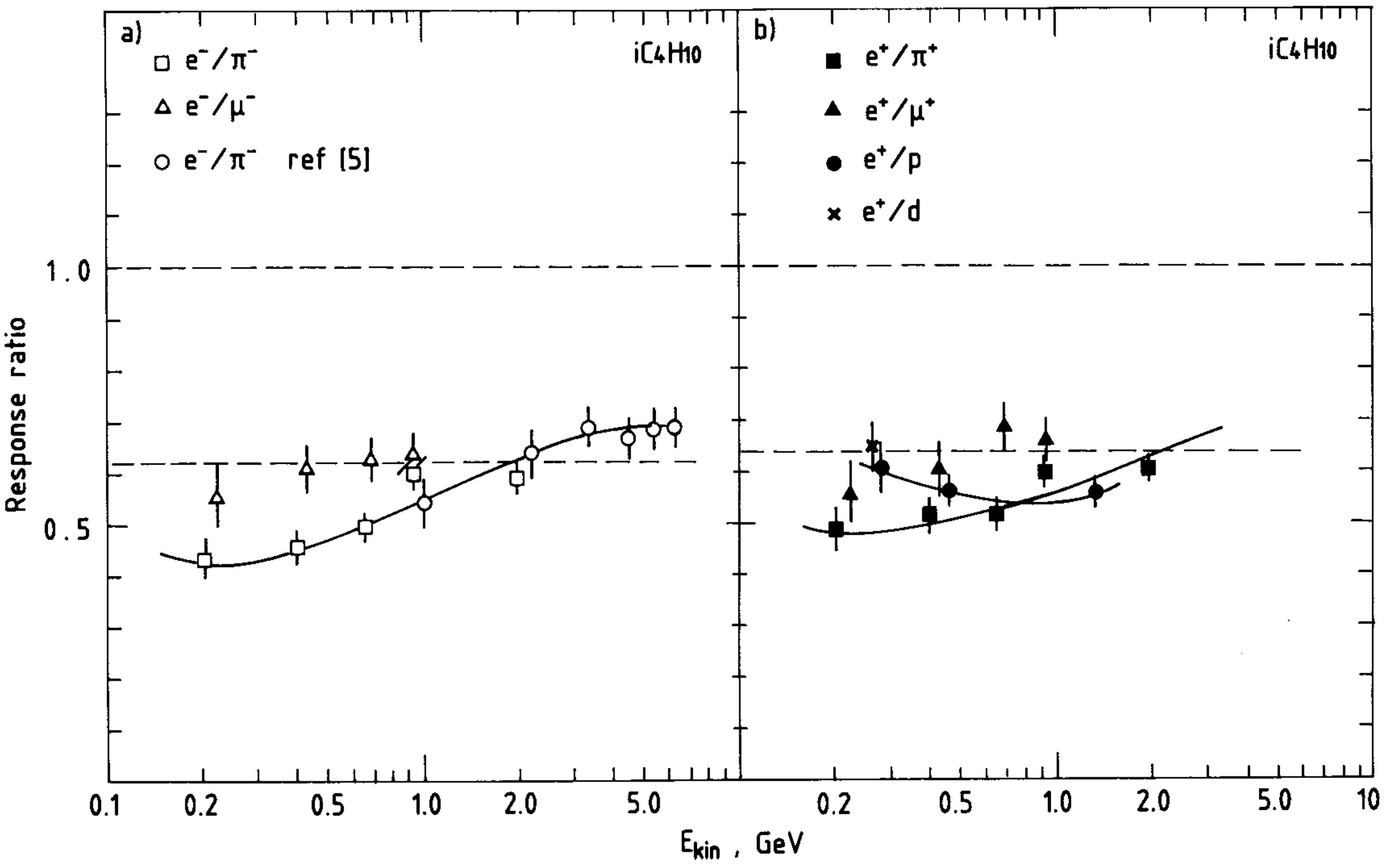
a)
□ e⁻/π⁻
△ e⁻/μ⁻
○ e⁻/π⁻ ref [5]
iC4H10
b)
■ e⁺/π⁺
▲ e⁺/μ⁺
● e⁺/p
× e⁺/d
iC4H10
Response ratio
1.0
0.5
0.1
0.2
0.5
1.0
2.0
5.0
10
E_kin , GeV

Fig. 16

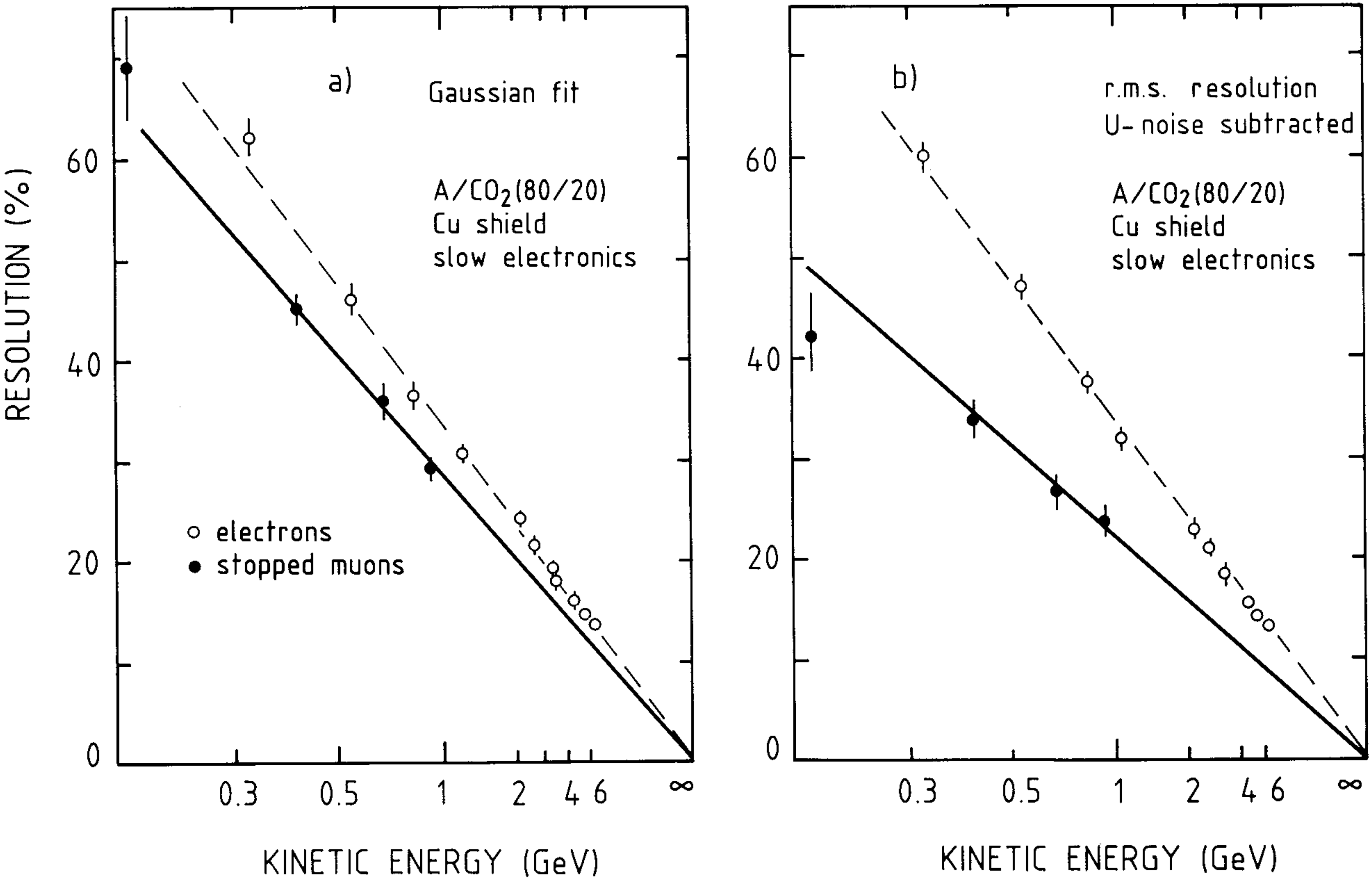
a)
Gaussian fit
A/CO$_2$(80/20)
Cu shield
slow electronics
○ electrons
● stopped muons
b)
r.m.s. resolution
U- noise subtracted
A/CO$_2$(80/20)
Cu shield
slow electronics
RESOLUTION (%)
0
20
40
60
0.3
0.5
1
2
4 6
∞
KINETIC ENERGY (GeV)

Fig. 17

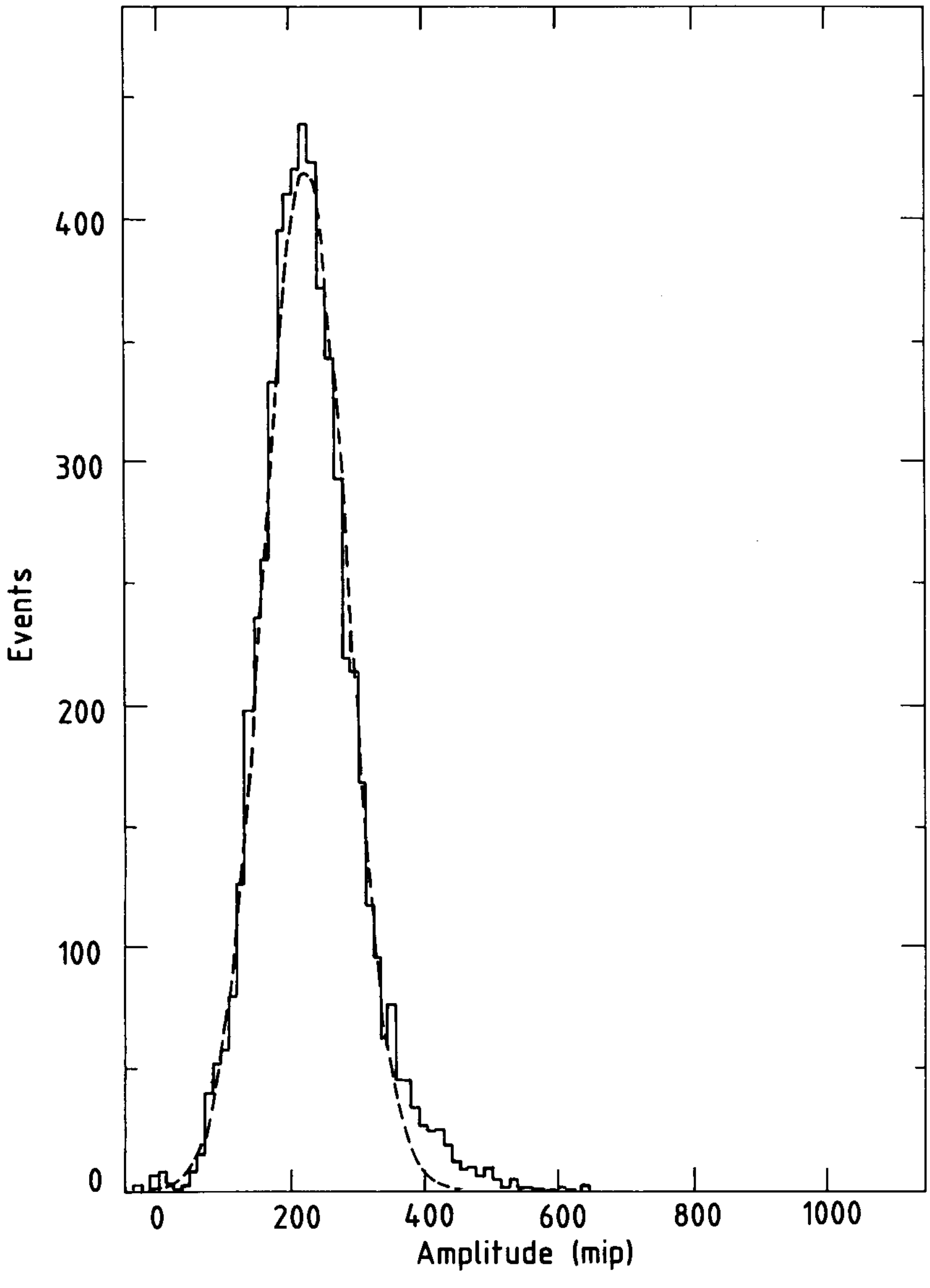

Fig. 18

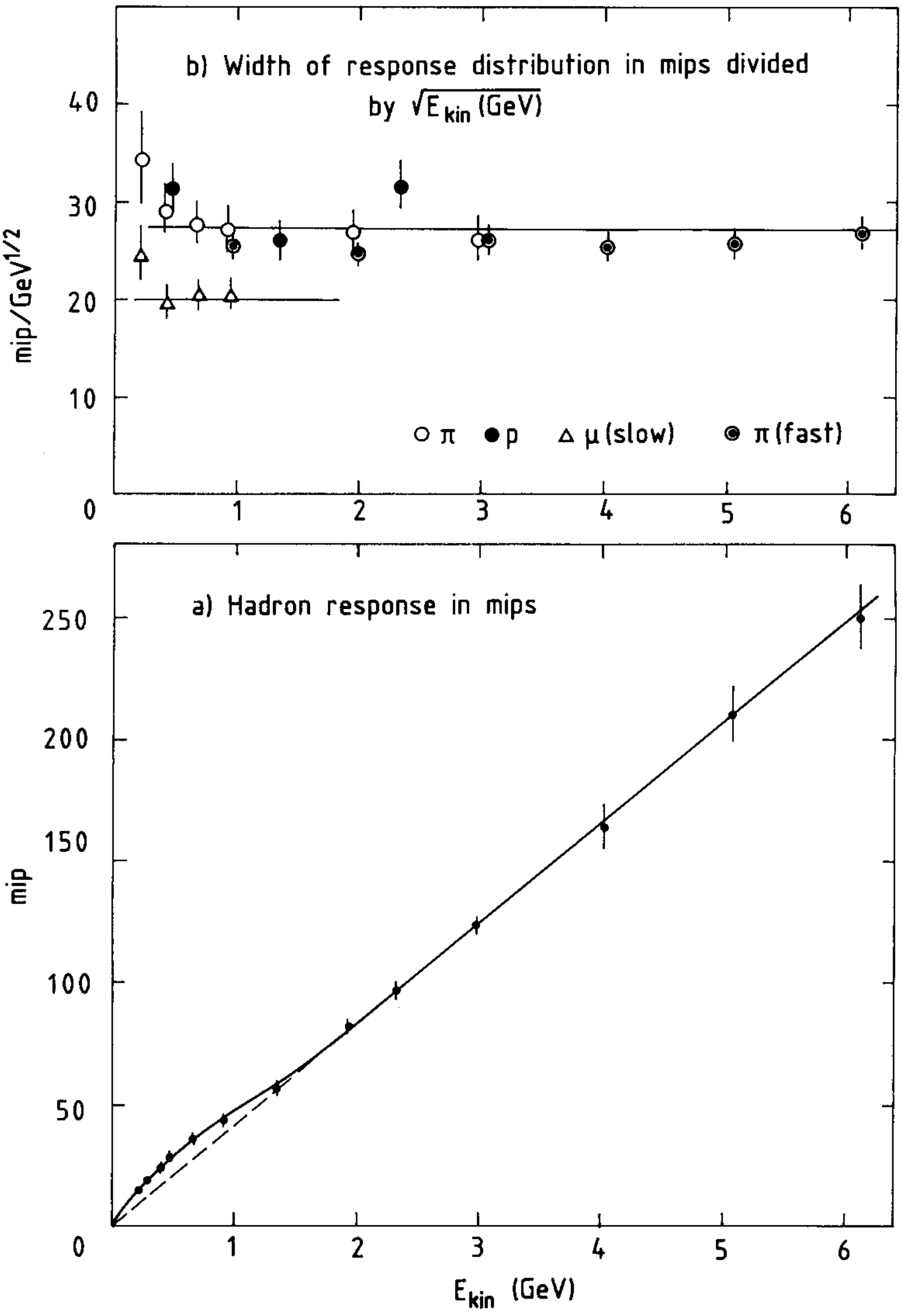
b) Width of response distribution in mips divided by $\sqrt{E_{kin}}$ (GeV)
mip/GeV$^{1/2}$
40
30
20
10
0
○ π
● p
△ μ (slow)
◉ π (fast)
1
2
3
4
5
6
a) Hadron response in mips
mip
250
200
150
100
50
0
1
2
3
4
5
6
E_{kin} (GeV)

Fig. 19

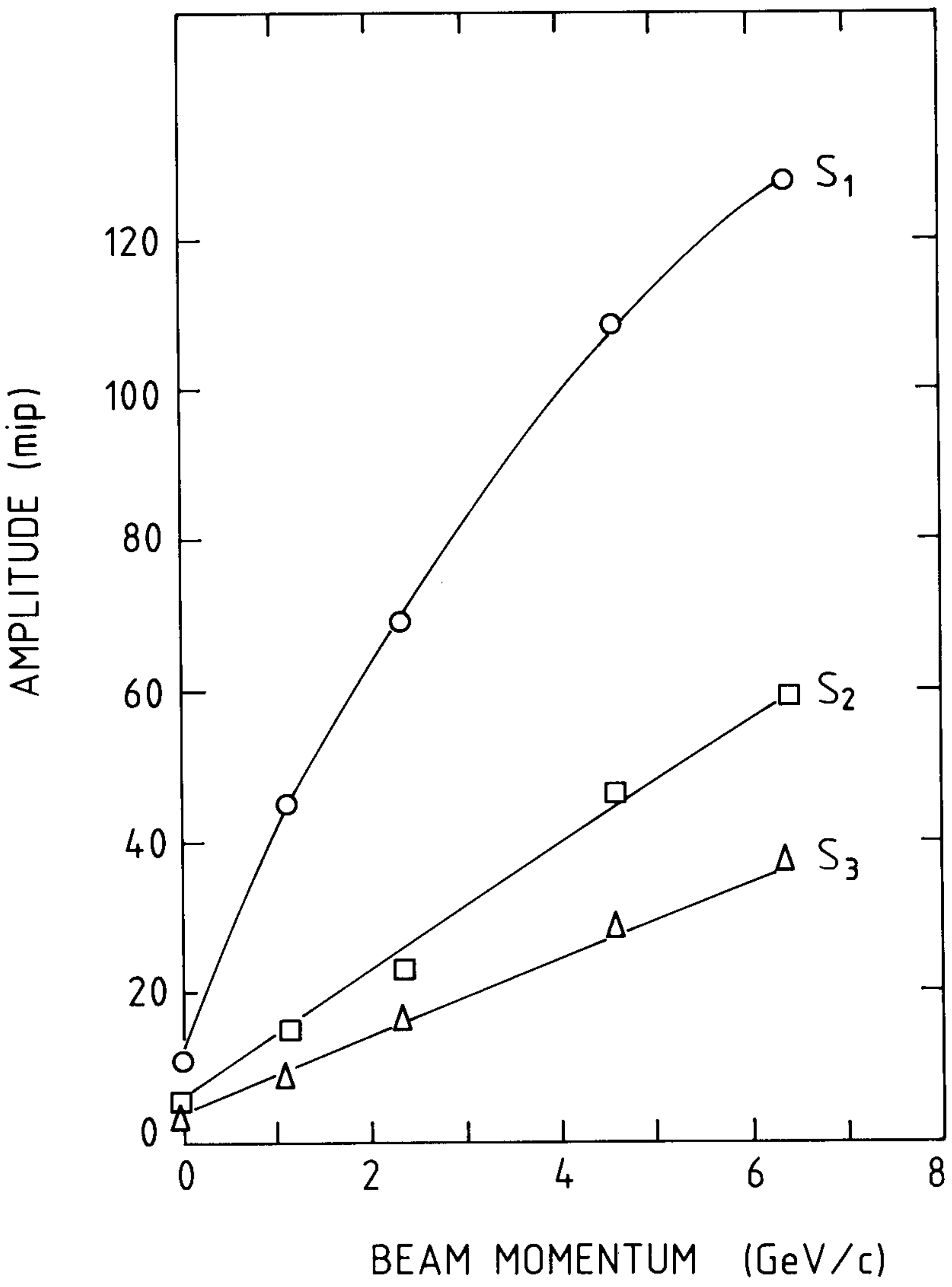
AMPLITUDE (mip)
0
20
40
60
80
100
120
0
2
4
6
8
BEAM MOMENTUM (GeV/c)
S_1
S_2
S_3

Fig. 20

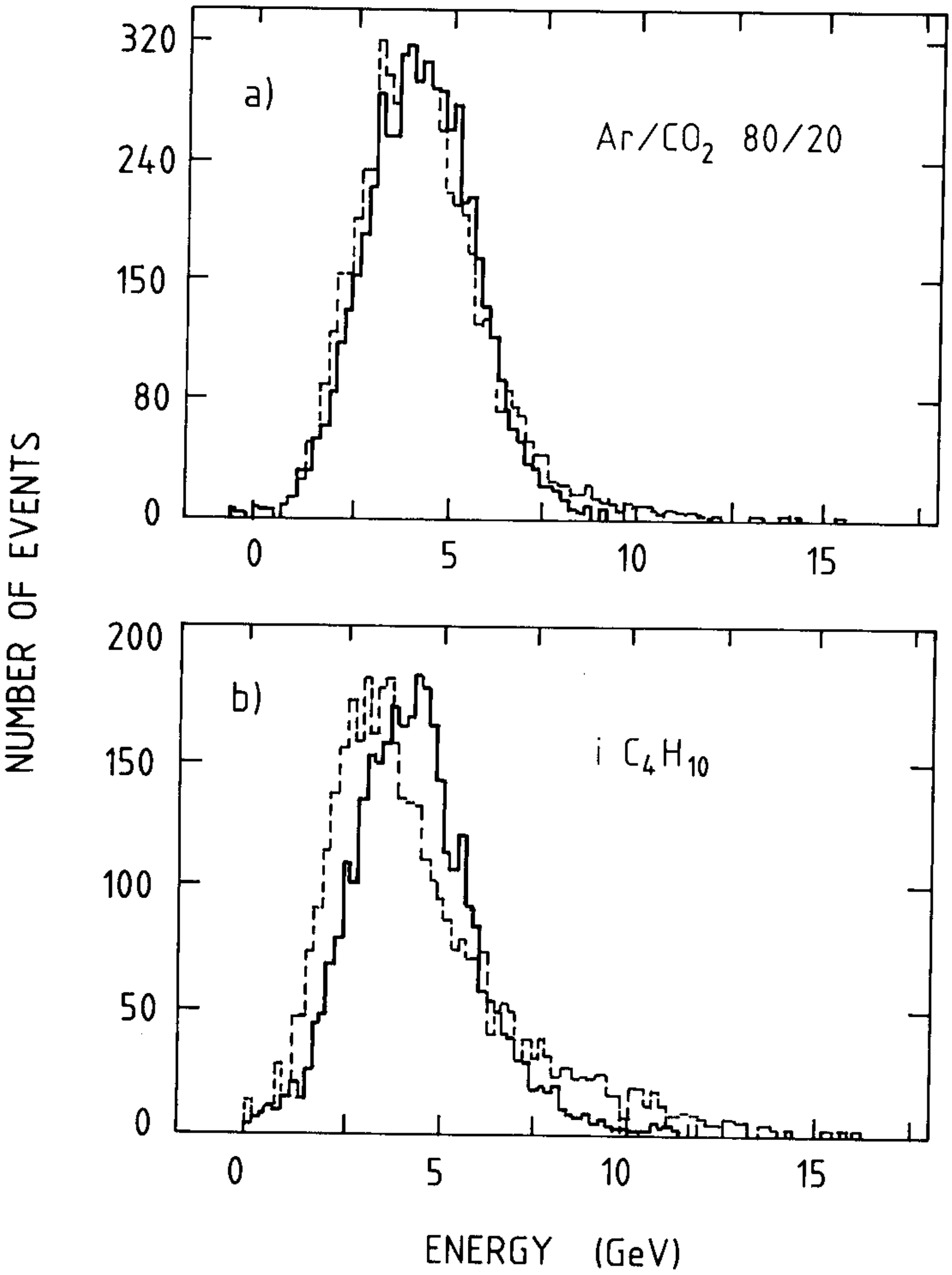
NUMBER OF EVENTS
a)
Ar/CO_2 80/20
320
240
150
80
0
0
5
10
15
b)
i C_4H_{10}
200
150
100
50
0
0
5
10
15
ENERGY (GeV)

Fig. 21

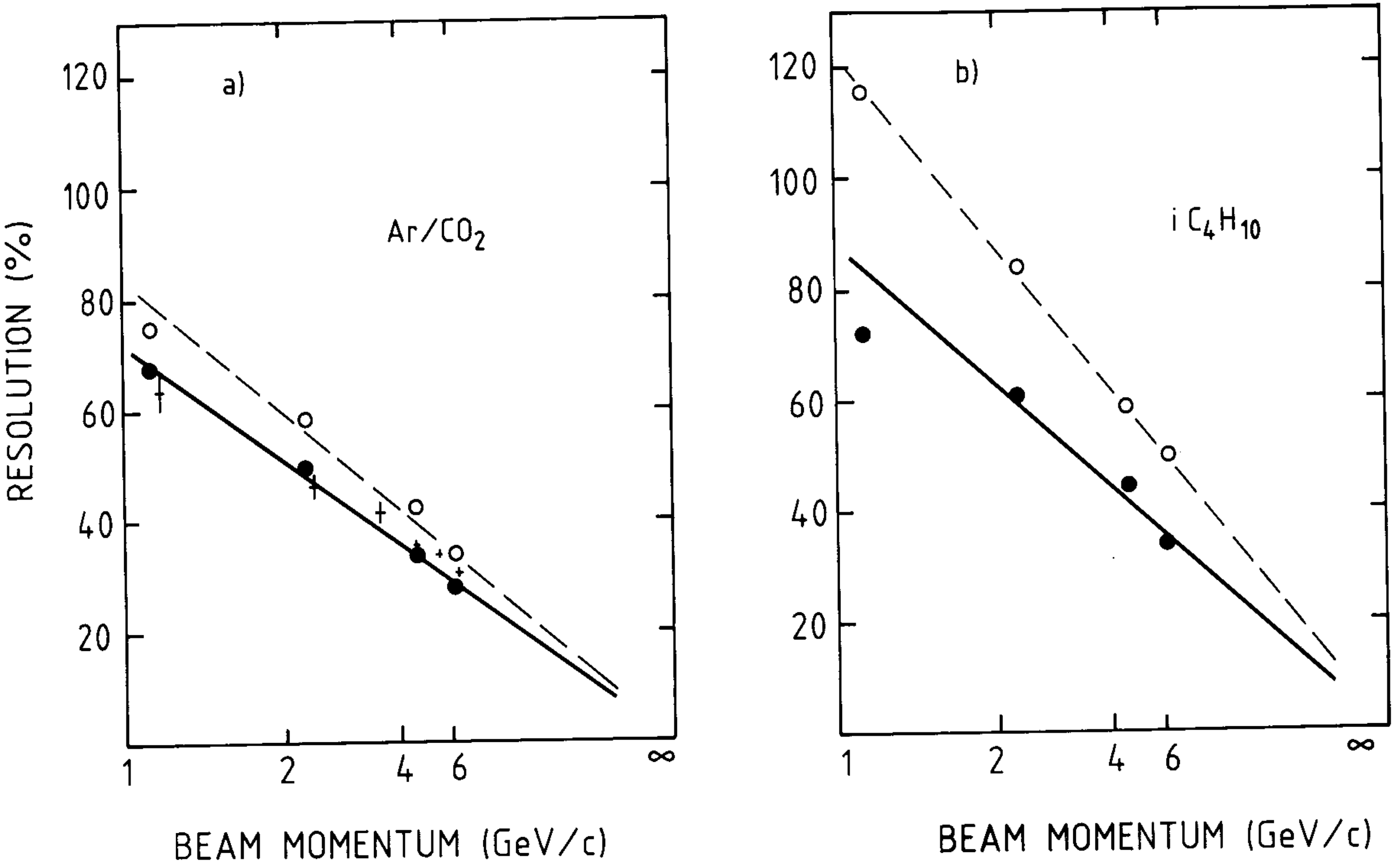
a)
Ar/CO$_2$
RESOLUTION (%)
120
100
80
60
40
20
1
2
4
6
∞
BEAM MOMENTUM (GeV/c)
b)
i C$_4$H$_{10}$
120
100
80
60
40
20
1
2
4
6
∞
BEAM MOMENTUM (GeV/c)

Fig. 22

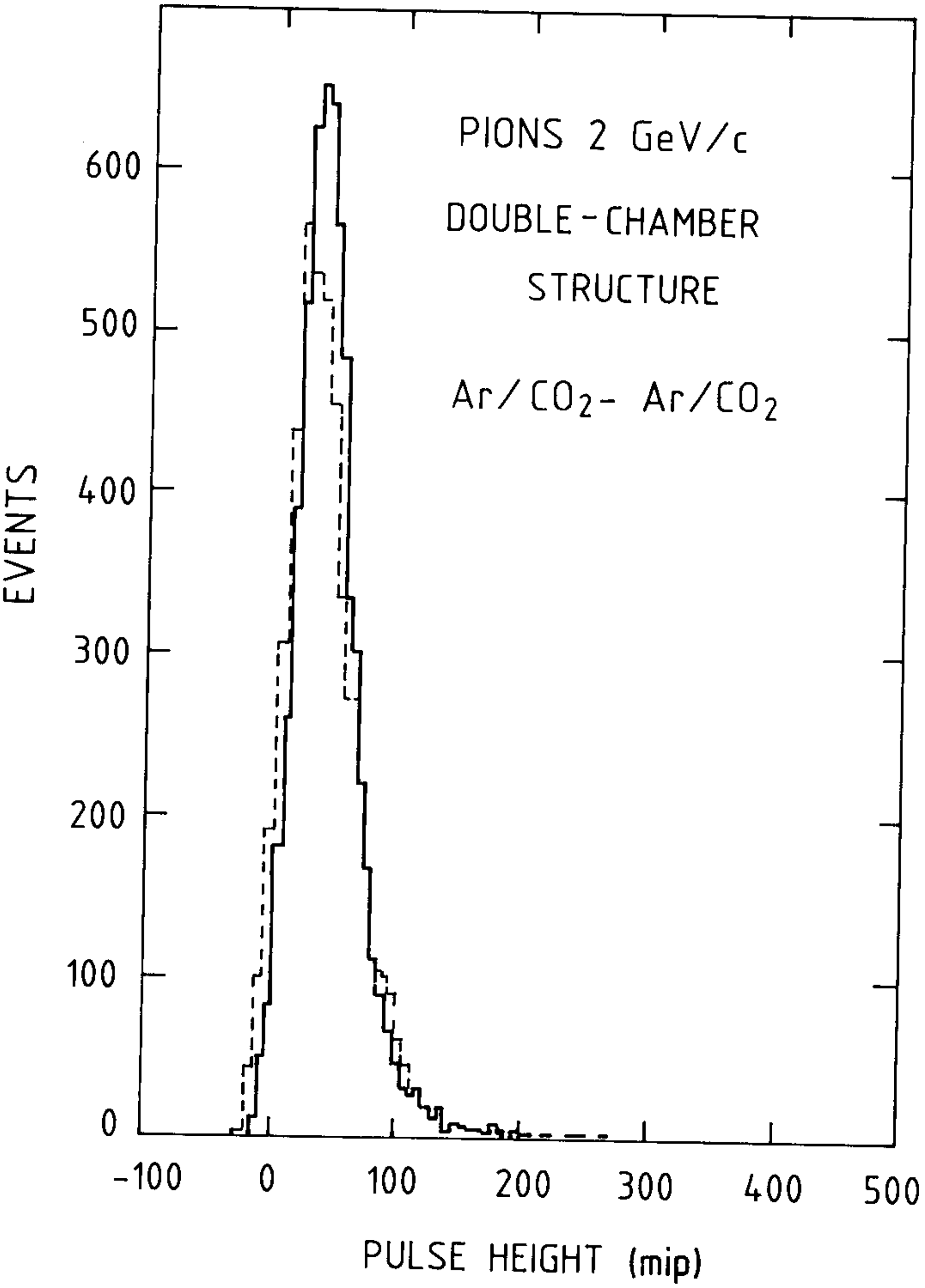
PIONS 2 GeV/c
DOUBLE-CHAMBER STRUCTURE
Ar/CO2- Ar/CO2
EVENTS
600
500
400
300
200
100
0
-100
0
100
200
300
400
500
PULSE HEIGHT (mip)

Fig. 23

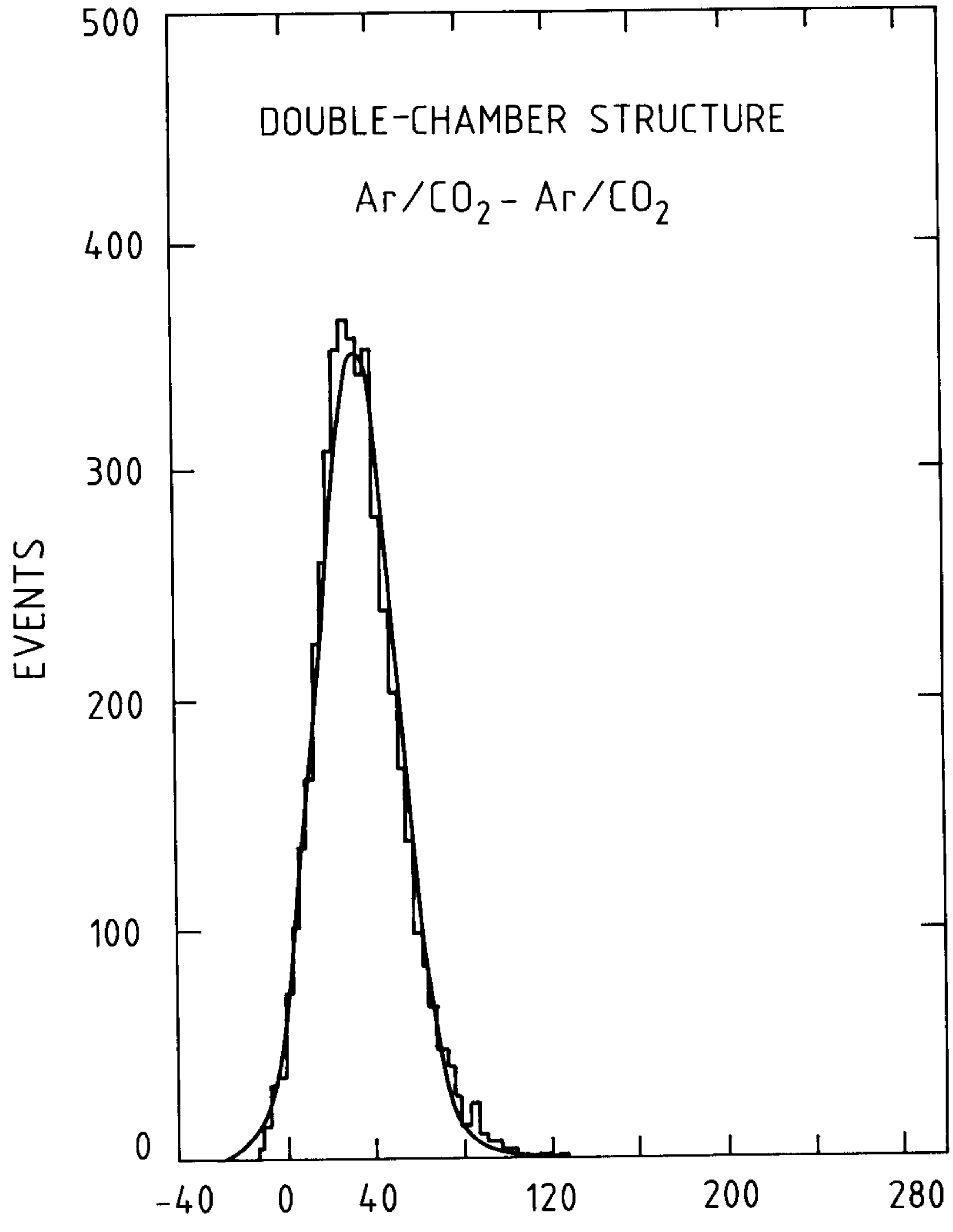
DOUBLE-CHAMBER STRUCTURE
Ar/CO_2 - Ar/CO_2
EVENTS
500
400
300
200
100
0
-40
0
40
120
200
280
PULSE HEIGHT (mip)

Fig. 24

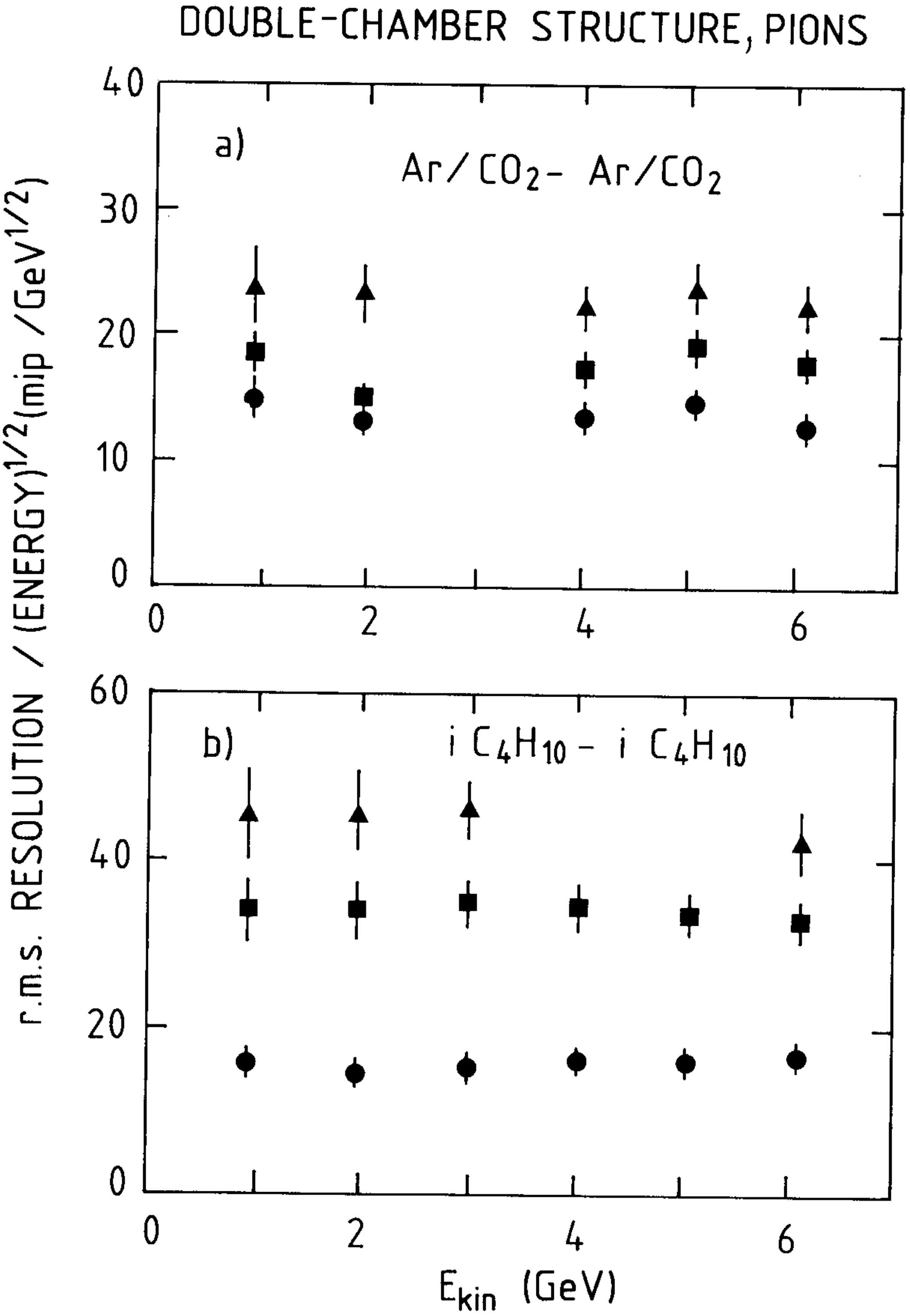
DOUBLE-CHAMBER STRUCTURE, PIONS
a)
$Ar/CO_2 - Ar/CO_2$
b)
$i\ C_4H_{10} - i\ C_4H_{10}$
r.m.s. RESOLUTION / (ENERGY)$^{1/2}$ (mip / GeV$^{1/2}$)
0
10
20
30
40
60
0
2
4
6
E_{kin} (GeV)

Fig. 25

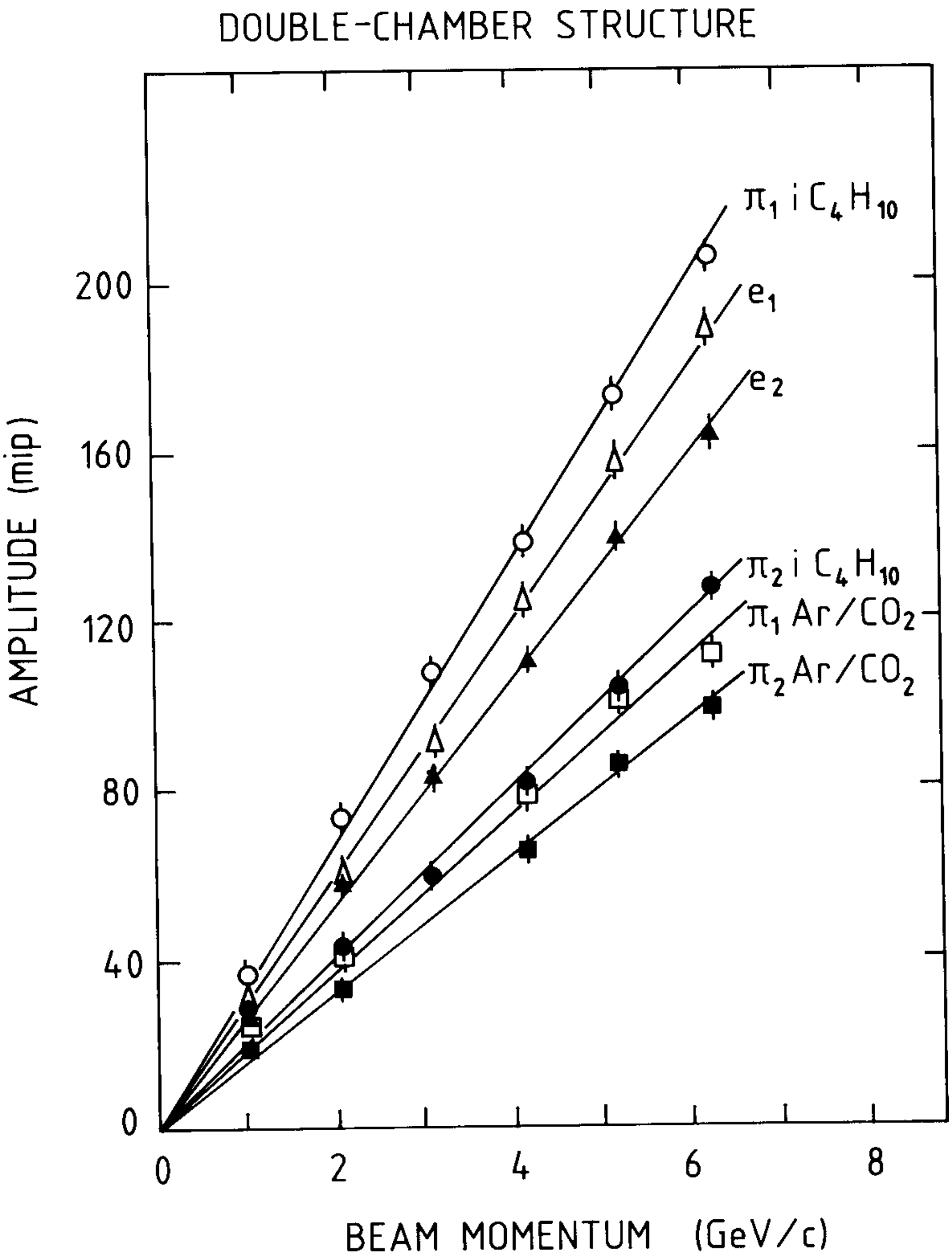
DOUBLE-CHAMBER STRUCTURE
AMPLITUDE (mip)
0
40
80
120
160
200
BEAM MOMENTUM (GeV/c)
0
2
4
6
8
π_1 i C_4H_{10}
e_1
e_2
π_2 i C_4H_{10}
π_1 Ar/CO_2
π_2 Ar/CO_2

Fig. 26

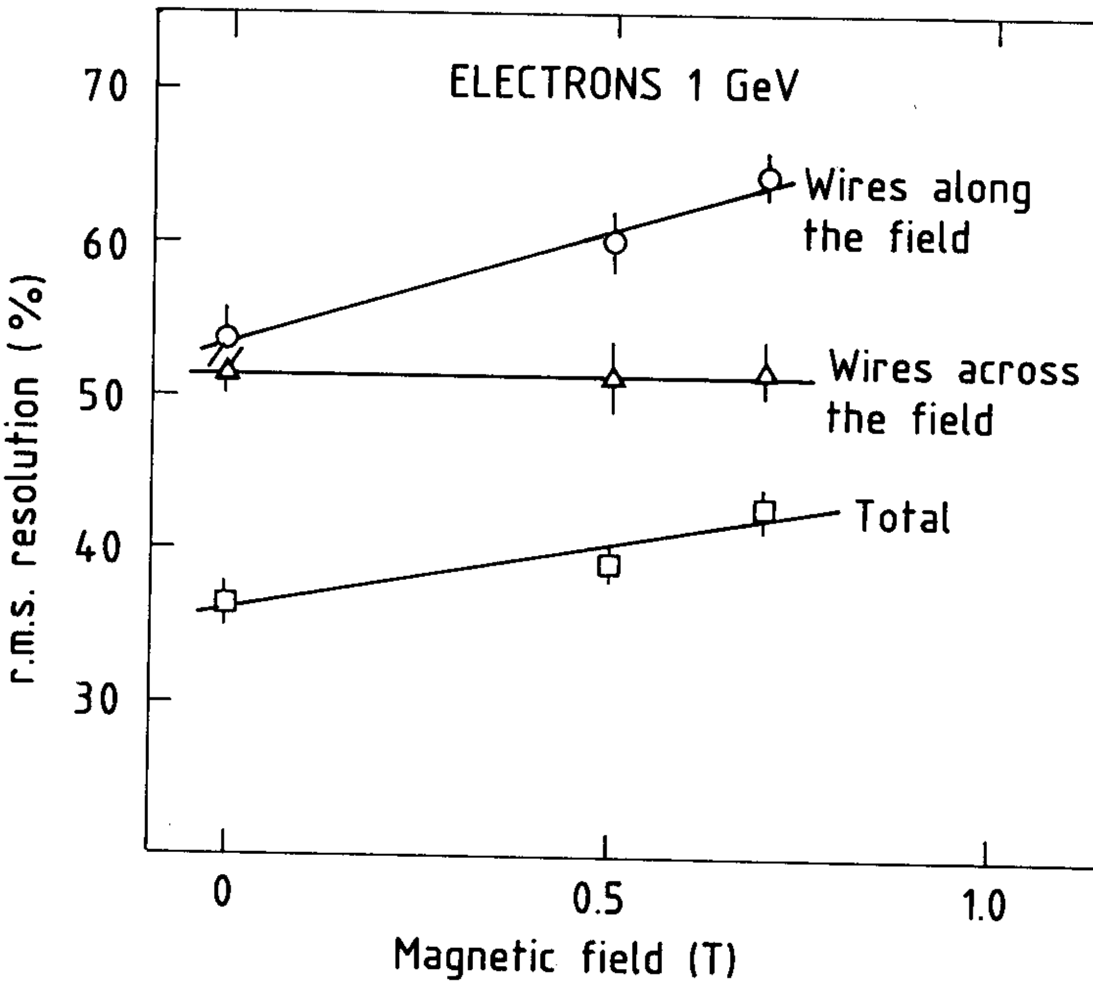
ELECTRONS 1 GeV
Wires along the field
Wires across the field
Total
r.m.s. resolution (%)
70
60
50
40
30
0
0.5
1.0
Magnetic field (T)

Fig. 27

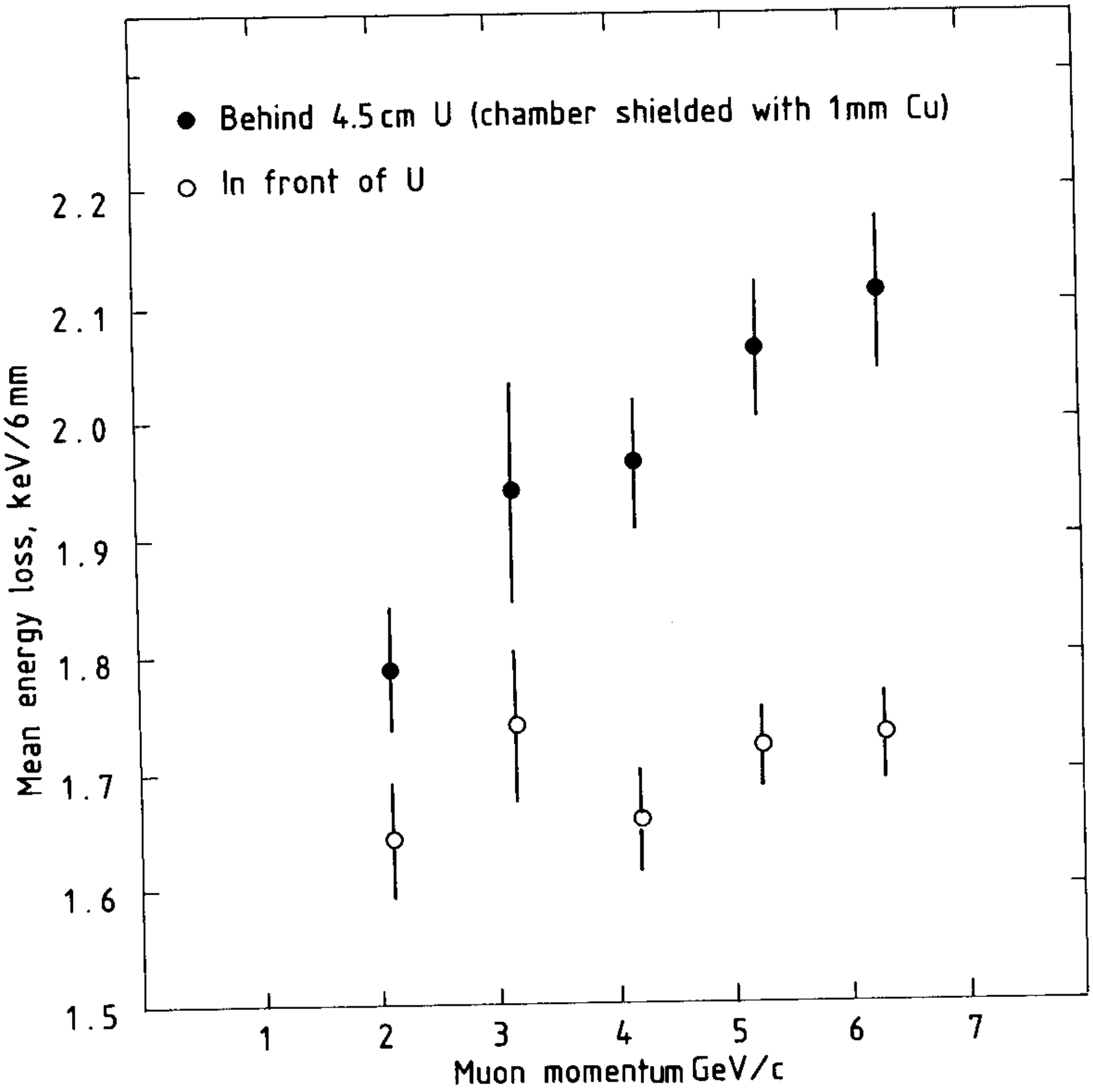● Behind 4.5 cm U (chamber shielded with 1 mm Cu)
○ In front of U
Mean energy loss, keV/6 mm
2.2
2.1
2.0
1.9
1.8
1.7
1.6
1.5
1
2
3
4
5
6
7
Muon momentum GeV/c

Fig. 28

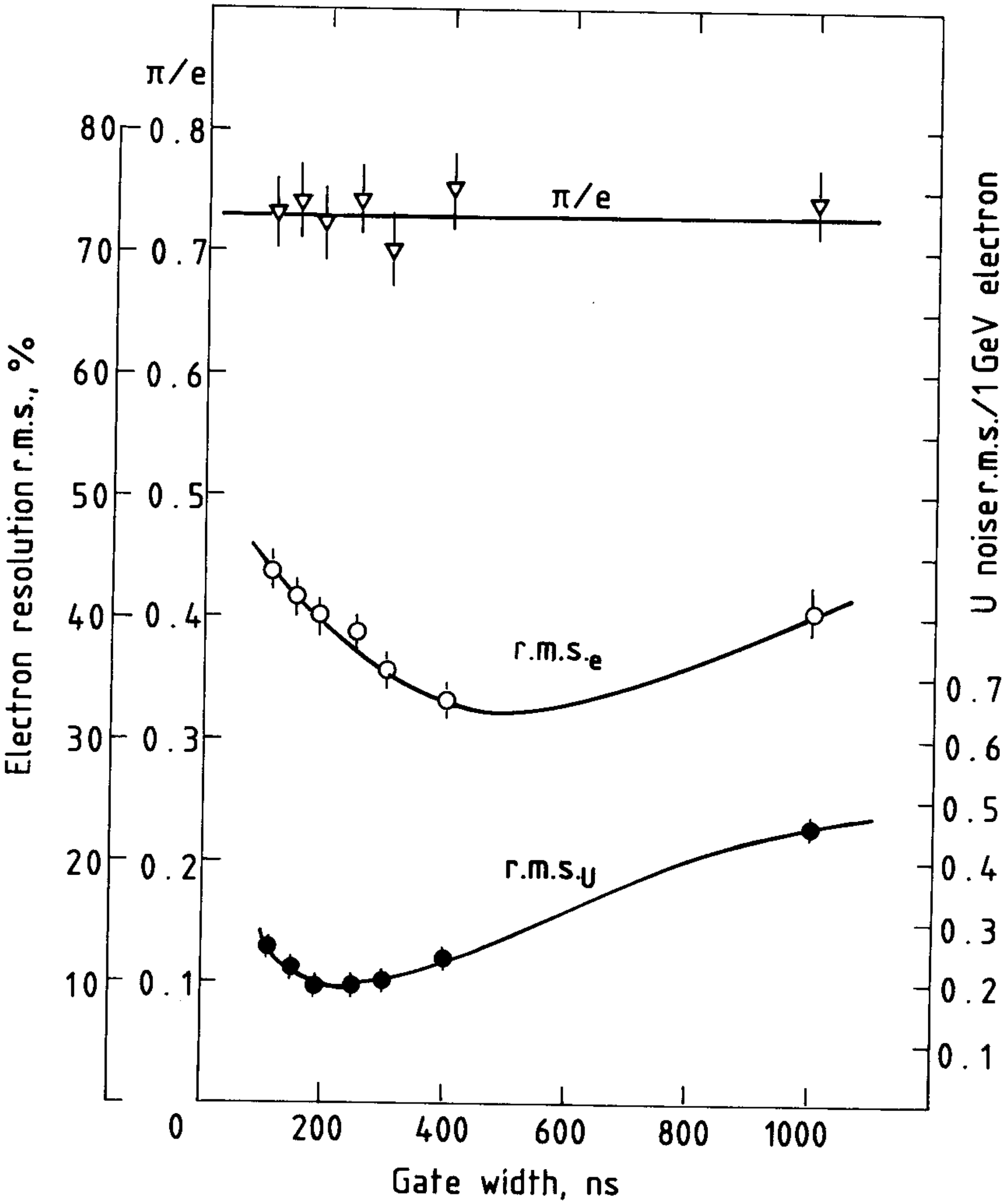
π/e
80
70
60
50
40
30
20
10
0
0.8
0.7
0.6
0.5
0.4
0.3
0.2
0.1
Electron resolution r.m.s., %
π/e
r.m.s.$_e$
r.m.s.$_U$
U noise r.m.s./1 GeV electron
0.7
0.6
0.5
0.4
0.3
0.2
0.1
200
400
600
800
1000
Gate width, ns

Fig. 29

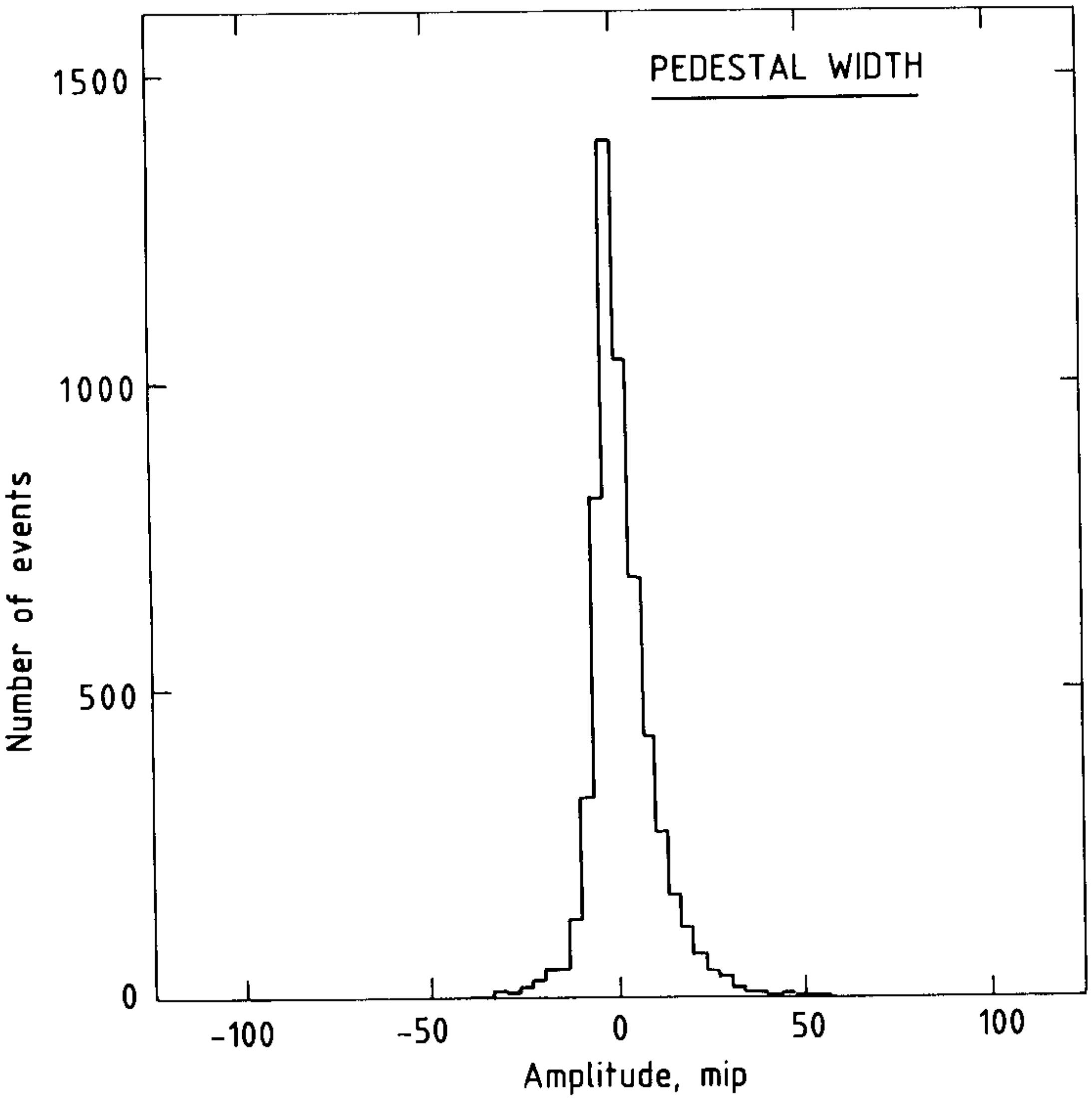
PEDESTAL WIDTH
1500
1000
500
0
Number of events
-100
-50
0
50
100
Amplitude, mip

Fig. 30